

Politecnico di Milano

Department of Aerospace Science and Technology
Master's degree in Aeronautical Engineering



Master Thesis

A Review of Numerical Models for the Simulation of Cavitating Flows in Hydrofoils

Advisor: Prof. Federico Piscaglia
Ing. Federico Ghiodi

Candidate:
Vayshnu Kasi
No. 941780

Academic year 2020-2021

Abstract

The present document investigates the cavitation phenomenon occurring in hydrofoils by means of a multiphase solver available in the open-source computational fluid dynamic (CFD) software OpenFOAM®. The current study uses the Reynolds Average Navier-Stokes methods to numerically simulate sheet/cloud cavitation around a NACA0012 hydrofoil with a fixed cavitation number $\sigma=0.8$. The turbulence model $k-\omega$ sst is applied in this thesis to limit the computational effort. However, multiple refined grids are accounted to compare the obtained solutions. Simulation results including cavitation form, lift, and drag coefficients related to $k-\omega$ sst turbulence models are studied and compared with experimental results. Non-cavitating conditions are experienced for angles of attack ranging from 3.2° to 3.8° ; in that range the $k-\omega$ sst turbulence model performs well. When the angle of attack ranges from 4.1° to 5.0° , the $k-\omega$ sst model fails to predict cavitation shedding. When the angle of attack is between 5.7° and 8° , the $k-\omega$ sst model can reproduce cavitation shedding, but the numerical result is slightly inaccurate compared to experimental data. As a result, in the current analysis the $k-\omega$ sst model is unable to provide very accurate values of forces coefficient when the angle of attack is further increased. Such result is in accordance with the literature chosen as basis for this work. An advanced turbulence model is hence recommended to guarantee better results.

Abstract

OpenFOAM^{registered} / (CFD)
NACA0012
 $\sigma=0.8$.
k- ω sst
k- ω sst ; k- ω sst
3.2° 3.8° 4.1° 5.0° , k- ω sst 5.7°
8°, k- ω sst , k- ω sst

Contents

Abstract	iii
Abstract in Sanskrit	iv
1 Basics of Cavitation	9
1.1 Definition of cavitation	9
1.2 Tension in Liquid	9
1.3 Concept of Vapor Pressure	9
1.4 The Main Forms of Vapor Cavities	11
1.5 Cavitation Regimes	11
1.6 Introduction to Nucleation	11
1.7 Homogeneous Nucleation Theory	12
1.8 Concept of Cavitation Number	13
1.9 Viscous effect in cavitation inception	14
1.10 Types of Cavitation	15
1.10.1 Travelling Bubble Cavitation	15
1.10.2 Vortex Cavitation	15
1.10.3 Cloud Cavitation	16
1.10.4 Shear Cavitation	16
1.10.5 Attached/Sheet Cavitation	17
1.11 Three dimensional effect in hydrofoil	19
1.12 Main Effect of Cavitation in Hydraulics Performance	19
2 Theoretical Formulation	21
2.1 Governing Equations	21
2.1.1 Homogeneous bubbly flows	21
2.1.2 Governing equations	21
2.2 Basic bubble dynamic equation	22
2.2.1 Assumptions	23
2.2.2 Boundary and intial condition	23
2.2.3 Rayleigh-Plesset eqaution	24

2.2.4	Schnerr-Sauer mass transfer model	25
2.3	Introduction to Turbulence	25
2.3.1	Reynolds-average Navier-Stokes equation	26
2.3.2	$k-\omega$ sst turbulence model	26
2.3.3	Transport equation for the sst $k-\omega$ model	27
2.3.4	Near-wall treatment	28
2.3.5	Automatic wall treatment for $k-\omega$ sst turbulence model	29
3	Case setup	31
3.1	A test case	31
3.2	Computational domain	31
3.2.1	Boundary and initial condition	32
3.3	Grid study	33
3.4	Case folder setup	33
3.4.1	0 Folder	33
3.4.2	Constant folder	34
3.4.3	System folder	34
3.4.4	Postprocessing	36
4	Result discussion	38
4.1	Non cavitating steady flow	38
4.2	Cavitation unsteady flow	41
4.3	Conclusion	58

Introduction

Cavitation is a very complex two-phase flow phenomenon. It can have multiple negative impacts on hydraulic machines such as vibration due to pressure fluctuation, high acoustic emission, solid surface erosion, and a drop-down in mechanical performance. Therefore it is necessary to investigate the physical mechanism for controlling cavitation in engineering applications. A primary objective of this study is to simulate unsteady cloud shedding in cavitation and the re-entrant jet of a closed type partial cavity over a NACA0012 hydrofoil at different angles of attack with a fixed cavitation number. The cloud shedding phenomenon is reproduced by using the $k - \omega$ sst as a turbulence model and homogeneous multiphase flow model. The present study applies a mass transfer model developed by Schnerr and Sauer called the Schnerr Saucer model. In addition, the limitations of the $k - \omega$ sst turbulent model at higher angles of attack will also be discussed. The solver InterFoam in the OpenFOAM[17, 4] source code is used to validate the results by running a multiphase flow setup.

The work in reference paper [16] focused on a 3D Clark-Y hydrofoil by utilizing an improved filter-based turbulence model based on density correction to control the overprediction of turbulence viscosity. In contrast, without using the filter-based model, the overprediction of turbulent viscosity causes the re-entrant to lose momentum. As a result, the re-entrant jet was unable to cut the cavity interface, preventing cloud shed. The other influencing parameter is the maximum density ratio which could affect the mass transfer rate between the liquid and vapor. Due to the increase in the maximum density ratio, the mass transfer rate between the liquid and vapor phases increases. In addition, the cavity length, cavity depth, and thickness are significantly increased. A large vapor cavity volume can result from mass transfer from liquid to vapor at a high maximum density ratio. According to this article, two-equation turbulence models cannot be used to simulate large-scale cavitation shedding due to turbulent viscosity overprediction. The study concludes that the two-equation model does not perform well near the wall of hydrofoil where viscous flow dominates but shows favorable results away from the foil in the yplus outer region where inertia dominates. ANSYS was used for the simulation.

According to reference papers [12, 11], the simulations were conducted on the NACA66 hydrofoil, which explains the 3D effect of cavitation vortex interaction when cloud shedding occurs. The authors compare LES Wall Adapting the local eddy-viscosity model over the LES WALE model which has a better ability to reproduce the laminar to turbulent transition in comparison with LES Smagorinsky. The cavitation vortex interaction includes vortex stretching, vortex dilation (due to volumetric expansion/contraction) baroclinic torque term (due to misaligned pressure gradient and density gradient). The researchers concluded that, as cavitation grows, there is a strong vortex cavitation interaction in the shedding vapor cloud, and that the vortex stretching, dilation term is vital to the transition from 2D to 3D. As the shed vapor cloud collapses downstream and the attached cavity shrinks, the transition from 3D to 2D occurs. The attached cavitation and boundary layer becomes thin during this process. This transition will carry out after a regular interval. In comparing experimental pressure fluctuation to numerical pressure fluctuation, a shift in the result is due to the streamwise vortex (one reason) in the real flow setup, which cannot be added to the simulation. It is clear from this paper that the cavitation shedding condition is essential for producing cloud shedding in the simulation along with the 3D effect, and its contribution has an effect on the numerical result. The simulation was performed in ANSYS.

In reference [7, 6, 8] the work was validated in OpenFOAM on NACA66 hydrofoil. It compares two cavitation models, one being the Schneer-Sauer model and the other being the Zwart model with LES as a turbulent model. They concluded that the Schneer-Sauer model is more accurate than the Zwart cavitation mass transfer model for unsteady large-scale cavitation shedding. Additionally, the 3D study provides more detailed information about the unsteady shedding along the span-wise direction. This paper also assumes a homogeneous flow, so-called bubbles two-phase flow, for numerical analysis using the Rayleigh-Plesset equation, with no regard for surface tension and viscous damping. Another hypothesis made in this article is that condensation and vaporization are controlled by barotropic state law. Therefore, these ideas are the basis of the present work. As a result of these assumptions, the Schneer-Sauer model has been selected as a cavitation mass transfer model to account for a higher angle of attack on hydrofoils.

In reference [18] the work focuses on the comparison of $k - \omega$ sst with modified $k - \omega$ sst and LES Smagorinsky model on NACA0012 hydrofoil at a higher angle of attack 8° with fixed cavitation number σ . The authors concluded that at an angle of attack greater than 8° it is better to apply the LES model. On the other hand, if an angle of attack is less than 8° is better to use the modified $k - \omega$ sst turbulence model. The filtered-based model of $k - \omega$ sst in comparison with base $k - \omega$ sst does not show much difference in the result at an angle of attack of 8° . This paper's conclusion is incorporated into the thesis by using the $k - \omega$ sst as the base turbulence model for any angle of attack less than 8° . This paper's boundary conditions are used to determine the case set up in the current work. To evaluate the numerical results obtained from the present work, we used experimental results derived from this paper.

Partially closed types of the cavity are our concern. To understand partial closed and open type cavity, reference [13] in which the authors investigate unsteady cloud shedding in NACA0009 hydrofoil and they concluded that the re-entrant jet was not energetic in the open cavity but there was a turbulent reattachment. Alternatively the closed partial cavity, there is an energetic re-entrant jet with turbulence reattached. Here it shows that the minimum cavity thickness condition associated with cavity length is required to observe the re-entrant jet and cloud shedding. This phenomenon was also explained in [10].

In reference [1] the paper gives an important idea about the need of using an incompressible segregated PISO algorithm. According to this paper, the pressure equation needs some special attention to increase the numerical stability along with the mass transfer model affecting the velocity-pressure coupling while dealing with the incompressible implicit LES turbulence model. For this reason, it is better to neglect the effect of compressibility and non-condensable gases. This paper also mentions the computational difficulty in using the LES turbulence model as it requires large computational power and cost. LES also requires a very fine mesh with a high computational burden and it is very difficult to obtain a grid-independent solution [16] for 3D cases. But the thesis focused on 2D so it is better to use the $k - \omega$ sst model with the compressible segregated PIMPLE algorithm [18].

The basic understanding of the cavitation in hydrofoil and multiphase flow is studied and the content that supports this thesis is from reference textbooks [10, 2, 3], for introduction to turbulence refer to [15, 9], and to understand about OpenFOAM, please consider the OpenFOAM guide reported in [5]. In this document, the chapter1 will cover all the basic understanding of cavitation which is necessary to know what is happening in the simulation. Chapter 2 will cover the formulation required to run the simulation. It comprises formulation related to basic fluid dynamics and assumption-based fluid flow equations and equations related to turbulence. Chapter 3 includes case setup, geometry, mesh, boundary condition which are required to run the OpenFOAM simulation. Chapter 4 includes a result discussion where the postprocessing data from OpenFOAM are tabulated and compared with the experimental results. Finally, the conclusion is reported in chapter 5 where the results are concluded with the expert's suggestion who supports me to strengthen the work.

Chapter 1

Basics of Cavitation

1.1 Definition of cavitation

Cavitation occurs when the pressure is lower than the vapor pressure in a liquid medium at a given temperature. The formation of vapor bubbles is considered to be void space, a cavity, and a region of the fluid in which vapor exists are called cavities. These vapor cavities inside a homogenous liquid (in the absence of bubbles in the fluid stream) can occur in many different conditions based on the characteristics of liquids that vary depending on the flow configuration and the physical properties of the liquid.

According to Fran and Michel [10] "Cavitation can be defined as the breakdown of a liquid medium under very low pressure". This makes cavitation relevant to the field of continuum mechanics and it applies to cases in which the liquid is either statics or motion.

1.2 Tension in Liquid

Liquid tension is defined as the decrease of pressure P occurring at a constant temperature, which might be the pressure P below the saturation vapor pressure P_v . Basically, the magnitude at which the rupture occurs is the tensile strength of the liquid, represented by ΔP_C , and the value of $(P_v - P)$ is the tension in the fluid, represented as ΔP . Often, cavitation refers to the rupture of a liquid at a roughly constant temperature. The maximum negative pressure at which water gets ruptured (in the absence of dissolved gas) varies between $-3 \cdot 10^9$ to $-3 \cdot 10^{10}$ kg/ms 2 .

1.3 Concept of Vapor Pressure

The concept of vapor pressure from the classical thermodynamic viewpoint in the phase diagram of water is shown in (Figure 1.1). Figure (1.1) shows that the curve from the triple point T_r to critical point C separates the liquid and vapor domains. The condition of evaporation or condensation of the fluid at a pressure P_v is known as vapor pressure and this is the function of temperature T . Cavitation in the liquid occurs by lowering the pressure at a constant temperature as often happens in real fluids. Thus cavitation appears similar to boiling, with exception of the fact that the driving mechanism is not the temperature but the pressure change. So the path in the phase diagram is said to be isothermal.

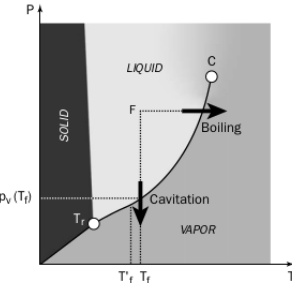


Figure 1.1: phase diagram[10]

Several steps can be distinguished during the first instants of cavitation:

- breakdown or void creation,
- filling of this void with vapor,
- eventual saturation with vapor.

In reality, the phases are simultaneous with the second step, so instantaneous saturation of the void with vapor can be justifiably assumed. It should be kept in mind that from the phase diagram the curve $P_v(T)$ is not an absolute boundary between liquid and vapor states. Deviation from this curve can also make the water not change its phase, even if a drop in pressure well below the vapor pressure occurs. This was explained by Andrews-isotherms (Figure 1.2) in the p-v diagram; the curves can be approximated in the liquid and vapor domains by the van der Waals equation of state. The transformation from liquid to vapor along the path AM can be avoided, because the liquid is in metastable equilibrium and it can even withstand negative absolute pressure i.e, tension, without any phase change. When treating water in such cases, special care must be taken.

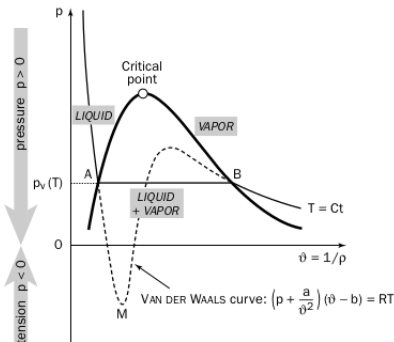


Figure 1.2: Andrews-isotherms[10]

In summary, Cavitation may or may not occur regardless of whether the local absolute pressure is equal to or less than the vapor pressure at the given global system temperature. The reason for this is because fluids have a metastable equilibrium. This difference between the vapor pressure and absolute local pressure at cavitation inception (the first point about which phase changes start to generate vapor bubbles) is called static delay. In some cases, there is also dynamic delay associated with inertial phenomena with the time necessary for vapor cavities to be observable.

1.4 The Main Forms of Vapor Cavities

Cavitation patterns of vapor structures can be divided into three forms. These are:

- Transient isolated bubbles: These appear in the region of low pressure well below the vapor pressure as a result of the rapid growth of very small air nuclei present in the liquid. They are carried along the stream and modify the flow. As they enter into a region of high pressure they progressively disappear.
- Attached or Sheet Cavities: Such cavities are often attached to the leading edge of the body.
- Cavitating Vortices: Cavitation can appear in the low-pressure core of the vortices in the turbulent wake.

Some vapor structures with a short lifetime that appear on the surface of the foils or propeller blades do not fall under these three forms; even though they have the form of attached cavities, they are transported similarly to traveling bubbles. This type of form is relevant for the present work.

1.5 Cavitation Regimes

For practical purposes, it is necessary to classify the cavitation region.

- Cavitation Inception: The limiting regime between the non-cavitating condition and the cavitating flow.
- Developed Cavitation: There is an extent of the cavitation zone or significant fall in the performance of the machines.

In the present work, we are mainly concerned about the extended region of the cavitation zone where there will be a high influence on unsteady cavitation shedding. The influencing situation that is favorable for the cavitation is wall geometry that gives rise to the local increment in the velocity with the drop in local pressure, and shear flows due to large turbulent pressure fluctuations.

1.6 Introduction to Nucleation

Small gas or vapor inclusions present in a liquid medium act as points of weakness. These are known as cavitation nuclei. During the experiment, this point of weakness acts as a starting point for the liquid to begin to break down, and it is a few micrometers to several hundred micrometers in diameter. They remain spherical at this scale due to surface tension. There are two types of nucleation:

- Homogeneous nucleation: When the pressure is well below the saturation pressure the liquid form temporary, microscopic voids that can constitute the nuclei, necessary for rupture and growth of bubbles.
- Heterogeneous nucleation: Nucleation can happen at the liquid-solid boundary, or as a result of contaminant very small sub-micron sized particles in the liquid, or as a result of contaminant gas particles as micro-sized bubbles that can be found in crevices within the solid boundary, within suspended particles, or freely suspended in the liquid, causing weakness in the fluid under operation.

Kinetic theories have also been developed to cover such heterogeneous nucleation and allow us to evaluate whether the chance that this will occur is larger or smaller than the chance of homogeneous nucleation. Another effect is called cosmic radiation which has less impact on contributing nucleation in a fluid medium. The cosmic radiation i.e. the collision of molecules due to high energy photon cause nucleation, but it has little chance to occur so we neglect these effects. In most cases, heterogeneities inside the homogeneous medium is taken into consideration because it is inevitable.

One must not forget that it is impossible to completely remove contaminated gas from water, so this effect must be taken into account. Numerical simulations cannot include this point of weakness, so external parameters have to be implemented to mimic these effects. It is for this reason that cavitation number and cavitation inception have been introduced in this work. These non-dimensional numbers can be extracted through experiments.

1.7 Homogeneous Nucleation Theory

This theory is the basic understanding of the Rayleigh-Plesset equation which is a basic traveling bubble transport equation that will be explained further.

Consider a spherical microbubble, containing gas and vapor (heterogeneous nuclei over homogeneous nuclei) in equilibrium within the liquid at rest. The liquid can withstand negative pressure which means that is in a metastable state according to the Andrews-isotherm curve (Figure 1.2). The bubble radius R is sufficiently small so that the hydrostatic pressure $2\rho g R$ can be neglected in comparison with surface tension $2S/R$. This condition requires R to be smaller than the limiting value namely 2.7mm for water. To fulfill this condition the microbubble whose diameter is smaller than 0.5mm only are considered. The pressure can be uniform in the bulk of the surrounding fluid where there is the bubble and this microbubble is spherical. The spherical shape in the bubble is mainly due to the surface tension which states that "intermolecular forces that tend to hold the molecules together and prevent the formation of the large hole".

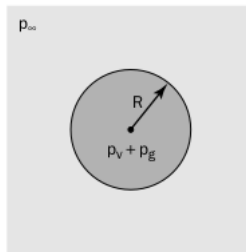


Figure 1.3: Microbubble in liquid [10]

The pressure equilibrium of the interface between the fluid surrounding and bubble surface is given by:

$$P_{\infty} = P_g + P_v - \frac{2S}{R} \quad (1.1)$$

P_{∞} is the surrounding bulk uniform pressure, P_g gas pressure inside the bubble, P_v vapor pressure, S surface tension, R radius of the bubble.

It is assumed that pressure change is slow enough to achieve mechanical equilibrium. However, the change in pressure must be rapid enough to ensure the gas diffusion at the interface is negligible. In other words, the transformation is assumed to be isothermal and the mass of the gas inside the bubble is constant. For the initial state, denoted by subscript 0, equation(1.1) is written as follows:

$$P_{\infty 0} = P_{g0} + P_{v0} - \frac{2S}{R_0} \quad (1.2)$$

As the gas pressure is inversely proportional to the volume in the isothermal transformation, then from equation (1.1) one can obtain:

$$P_\infty = \frac{P_{g0}}{[R_0/R]^3} + P_v - \frac{2S}{R} \quad (1.3)$$

assuming that the critical nucleus is in thermodynamic equilibrium with its surrounding after its creation. The critical radius and critical pressure are given by comparing equation (1.1) and (1.2) by assuming virtual transformation from initial radius to critical radius under the isothermal condition with the mass of gas. Two mechanisms take place in equation (1.1), they are:

- the internal pressure effect which tend to increase the bubble size,to reach critical size.
- the surface tension effect which act in the opposite direction resulting in minimum extension are given by:

$$R_C = R_0 \frac{3P_{g0}}{[\frac{2S}{R_0}]^{1/2}} \quad (1.4)$$

$$P_C = P_v - \frac{4S}{3R_C} \quad (1.5)$$

The mass of gas inside the bubble is said to be constant and it is directly proportional to the $P_{g0}R_0^3$. To use the condition of a constant mass of gas either use one of the doublets (R_0, P_∞) , (R_0, P_{g0}) or preferably one of the quantities R_c or P_c . The stability of the nucleus is given in (Figure 1.4) in which the mechanical equilibrium of the specific nucleus is stable on the branch of the curve that has a negative slope. The other branch which is on the right side is said to be unstable.

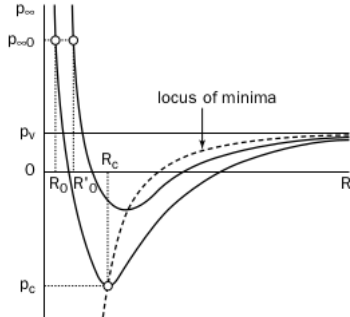


Figure 1.4: Equilibrium of a sphere nucleus [10]

1.8 Concept of Cavitation Number

The coefficient of pressure C_{pmin} for an ideal fluid is dependent on geometry when the effect of viscosity is included the C_{pmin} is also a function of Reynolds number R_e . For this instance just consider the C_{pmin} as a function of geometry only, which is stated in [2].

$$C_{px} = \frac{P_x - P_\infty}{0.5\rho U_\infty^2} \quad (1.6)$$

Cavitation occurs when the pressure is less than saturation pressure at a given temperature. This natural event can be formulated through a non-dimensional term called cavitation number σ . The cavitation number σ are related with the C_{pmin} thanks to the following.

$$\sigma = \frac{P_\infty - P_v(T_\infty)}{0.5\rho U_\infty^2} \quad (1.7)$$

The nucleation that will initially encounter at some point in the flow field is called cavitation inception for a sufficiently small value of σ (which means P_∞ is sufficiently smaller than P_v and U_∞ is sufficiently greater). The cavitation inception, also known as the lowest pressure point around which nucleation begins to form, appears to be observable. There is an increase in the formation of bubbles in the flow as σ is reduced more below σ_i .

$$\sigma_i = -C_{pmin} \quad (1.8)$$

From Figure (1.5), for $\sigma > -C_{pmin}$ the pressure along the entire trajectory is greater than vapor pressure P_v and still non-cavitating condition is respected. For $\sigma = -C_{pmin}$, the nucleus encounters $P = P_v$ only for an infinitesimal moment. Thus the observation of nuclei is limited or might not be observed. For $\sigma < C_{pmin}$, the nucleus experience $P < P_v$ for a finite time. Thus it is observable and they travel along the streamline.

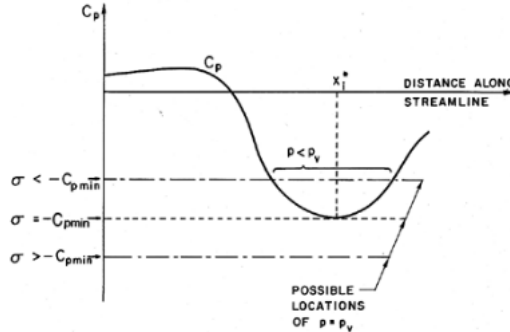


Figure 1.5: Schematic of pressure distribution on a streamline[10]

So far as free stream nuclei (heterogeneous nuclei) are concerned two main factors that cause σ_i be different from C_{pmin} . The first nucleation may not occur at $P = P_v$. In a degassed liquid, nucleation requires positive tension ΔP_c and hence nucleation would require the cavitation number $\sigma_i < C_{pmin}$, namely the equation relating the terms like C_{pmin} and tension of the fluid i.e. $\sigma_i = -C_{pmin} - \frac{\Delta P_c}{0.5\rho U_\infty^2}$. In a liquid containing great deal of contaminant gas ΔP_c could be negative so that σ would be larger than $-C_{pmin}$ under the condition $P < P_v - \Delta P_c$. This makes the $\sigma_i < -C_{pmin} - \frac{\Delta P_c}{0.5\rho U_\infty^2}$. All these conditions should respect the assumption of isothermal. If we include the temperature then σ_i will also be a function of Temperature. When there is a great deal of contaminant gas the tension of the fluid ΔP_c is negative. This means less tension and a rupture of fluid that occurs faster as the fluid tend to avoid the metastable equilibrium. In another sense, positive tension in the case of degassed fluid provides control in cavitation. So not only the geometry but also treating fluid for the experiment is also contributing to the cavitation.

1.9 Viscous effect in cavitation inception

In real fluid, C_{pmin} is not only the function of geometry but also the contribution by the viscosity. To include this effect of viscosity the C_{pmin} would be a function of Reynolds number, R_e so the cavitation

inception, σ_i is a dependence of Reynolds number R_e . In most engineering applications the flow is said to be turbulent so the vortices occur not only because of the inheritance of turbulence but also due to the free and forced shedding of vortices. This has major consequences in the cavitation inception σ_i because the pressure at the center part of the vortices is lower than the mean pressure in the flow. For this reason, the cavitation first occurs at the core and σ_i changes with R_e . There are a few other effects that make the σ_i to be more complicated in measurement through experiment:

- Existence of tensile strength can cause a reduction in σ_i .
- Residence time effects can cause a reduction in σ_i .
- Existence of contaminated gas can cause an increase in σ_i .
- Steady viscous effect due to dependence of C_{pmin} on R_e can cause σ_i to be function of R_e .
- Turbulence effect can cause an increase in σ_i

If these effects are not included then σ_i is the only function of C_{pmin} . Some of the experimental techniques which are used to measure the σ_i are based on acoustic scattering and light scattering. These have been used to measure the number of nuclei present in the liquid. Other instruments known as cavitation susceptibility meters cause a sample of liquid to cavitate and measure the number and size of the resulting microscopic bubbles. The discussion of this technique is out of the scope for this document.

1.10 Types of Cavitation

1.10.1 Travelling Bubble Cavitation

The bubble began as micron-sized nuclei in the liquid of the oncoming stream and the bubble moved with the flow free stream velocity close to the solid body. Cavitation inception was deemed to occur when the bubble reaches an observable size.

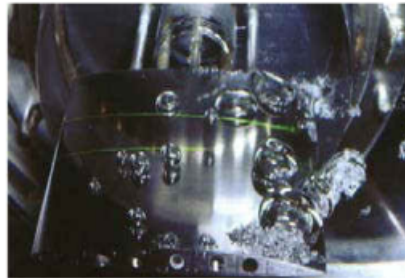


Figure 1.6: Travelling bubble on the surface of an hydrofoil [10]

1.10.2 Vortex Cavitation

This type of cavitation comes under large-scale cavitation structures. Cavitation inception often occurs at the core of the vortices when the core pressure is well below the mean flow pressure. For high R_e the vortices in a turbulent mixing layer or wake will also cavitate. This type is often seen in the tip vortices in the ship's propellers or pump impellers. The three-dimensional shedding of vortices from a finite aspect ratio foil often leads to the formation and propagation of a ring vortex with a vapor core.

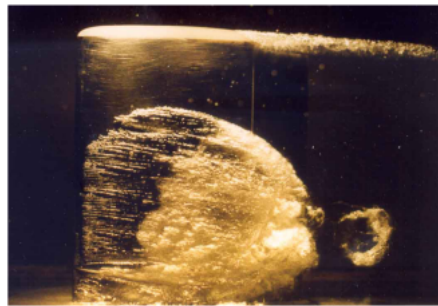


Figure 1.7: ring vortex on the surface of an hydrofoil [10]

1.10.3 Cloud Cavitation

This is another class of large-scale cavitation. The periodic formation and collapse of a cloud of cavitation bubbles are observed. This topic is more pertinent to the current project.

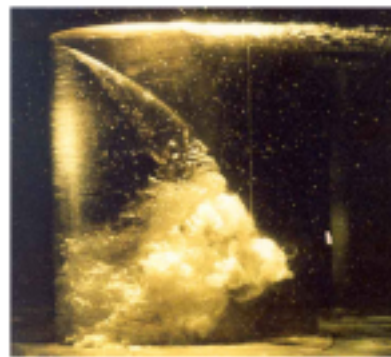


Figure 1.8: Cavitating cloud on hydrofoil [10]

1.10.4 Shear Cavitation

The region with high shear vorticity produces. As a result, a coherent rotational structure is formed and pressure levels drop in the core of the vortices which became the potential site for the cavitation. This often happen in the flow separation region which is developed by the hydrofoil at very high R_e and angle of attack.

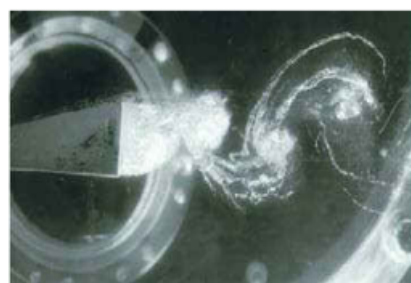


Figure 1.9: Shear Cavitation [10]

1.10.5 Attached/Sheet Cavitation

These types of cavitation are often experienced in hydrofoils. The present work focused on simulation of Attached/Sheetcavitation along with closed type partial cavitation through the case setup and this is the area of interest to replicate the unsteady behavior of cloud shedding.

SuperCavitation: As the cavitation parameter is decreased a small cavity attached to a hydrofoil will extend to grow longer and longer as can see in figure (1.10). The super cavity as soon as it ceases to close the cavitation wall but inside the liquid downstream of the cavitation. As a consequence, the lift of the foil will decrease with an increase in drag. For lower cavitation numbers which mean low R_e the supercavitation is experienced in the foil and cavity closure occurs at the rear part. Because of the low Reynolds number R_e laminar separation boundary layer will experience over the hydrofoil as the angle of attack increases. A well-developed cavity always detached downstream of the laminar separation of the boundary layer. The existence of separation, which generates a relatively dead zone near the downstream is the only way for the cavity to get attached to the wall i.e, turbulent reattachment. On the other hand, if there is no reattachment then the cavity will sweep away by the flow. In addition to turbulent reattachment, there is a cavity closure region near the downstream because the pressure inside the cavitation zone is less than surrounding freestream pressure. The unbalance inertia and pressure force gives a curvature oriented toward the cavity.

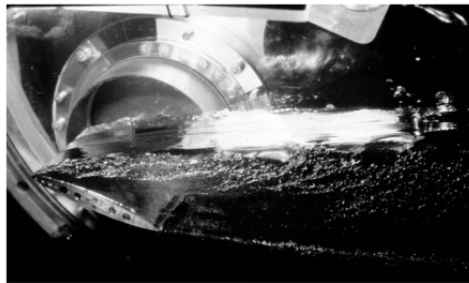


Figure 1.10: Supercavity behind two dimensional hydrofoil [10]

Partial Cavitation: In partial cavitation, the attached cavity closes on the suction side of the hydrofoil. This type of cavitation has two types:

Open attached cavity -partial type: From the reference [13], the authors investigate the NACA0009 hydrofoil under cavitation conditions. They concluded that an open attached partial type cavity is typically frothy in appearance and has periodically varying lengths, which is associated with the shedding of vapor clouds. Although recirculation flow related to the region of flow separation, i.e. turbulent reattachment, was recorded in the cavity closure, the re-entrant jet was not observed. The re-entrant jet in an open cavity is not observed due to conditions linked to the maximum cavity thickness, which is not reached in the open cavity. This is because there exists a low cavitation number associated with low angles of attack in the case of hydrofoils which can be seen in the figure(1.12).

Closed attached cavity-partial cavity: From the observation of authors [13], they concluded that this type of cavity has a relatively stable cavity length, a clear interface, and a cavity the closure that is relatively free from the bubble and entirely vapors fill. This demonstrates an important aspect of introducing the single-phase flow concept by considering the vapor-filled state, because bubble interaction is completely removed, as stated in the above statement of the closed partial cavity, and assuming the relative velocity between these two phases is zero, the flow now completely transfers to a single-phase flow regime. This simulation adapts closed type partial cavitation for unsteady cloud shedding and re-entrant jet observation.

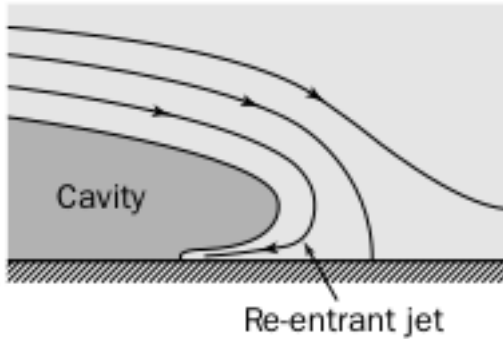


Figure 1.11: closure region of partial cavity [10]

Unsteady Re-entrant jet: The re-entrant jet proceeds from upstream, carrying a tiny amount of liquid inside the cavity, and the outside section is reattached by turbulent reattachment, as shown in figure (1.11). If the cavity interface is close to the suction rear side, where maximum cavity length is seen, a reentrant jet with an energetic flow will be able to cut the cavity interface when this re-entrant jet impinges on the cavity interface. It will induces a periodic break-off and roll-up of a part of the cavity. If the re-entrant jet moves far upstream, it causes a large portion of the cavity to break off then the process creates large-scale cloud shedding. If they move to a smaller distance upstream before impingement on the cavity surface then the process is called small-scale cloud cavitation.

From the figure(1.12) we can see that the open cavity at low cavitation and low angle of attack where the re-entrant is not observed or weak in re-entrant flow but there is a turbulent reattachment. At the same time in the periodic zone regime, we can see cloud shedding at a higher angle of attack and higher cavitation number along with the ratio of cavitation thickness to the chord e/c is minimum and the ratio of the length of the cavity to chord l/c is around half the length of the chord act as a maximum l/c i.e. a peculiar instability develops for partial cavities of medium length. On the other hand, it was limited by the minimum cavity thickness. Such limits suggest that a minimum value of cavity thickness is required for the periodic regime to develop. This also shows that cavity thickness must be larger than the re-entrant jet thickness for this instability to occur along with another condition like the periodic regime is bounded by the maximum value of the cavity length which indicates that instability should not occur for very long cavities. This condition also holds for the re-entrant jet which requires a minimum threshold value of the adverse pressure gradient to gain the impulse. Finally, to generate partial periodic cavity shedding and an energetic re-entrant jet, there must be a minimum cavity thickness to chord ratio and a maximum length of the cavity to chord ratio.

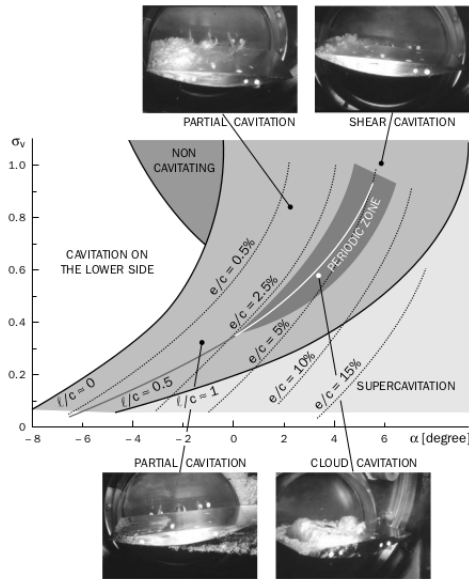


Figure 1.12: Main cavity patterns at $R_e = 2.10^6$ $V_\infty = 10m/s$ on plano-circular hydrofoil [10]

1.11 Three dimensional effect in hydrofoil

The transition of sheet cavitation to cloud cavitation can result in a highly unstable flow. To study cavitation-vortex interaction[12], the vorticity transport equation in a varying density flow is given as

$$\frac{D\omega}{Dt} = (\omega \cdot \nabla) \vec{V} - \vec{\omega}(\nabla \cdot \vec{V}) + \frac{\nabla \rho_m \times \nabla P}{\rho_m^2} + (\nu_m + \nu_t) \nabla^2 \vec{\omega} \quad (1.9)$$

In this equation, the first term on the right-hand side (RHS) is the vortex stretching term. The term describes the stretching and tilting of a vortex caused by velocity gradients. On the right, the second term is the vortex dilation term due to volumetric expansion or contraction, which describes how fluid compressibility affects vorticity. The third term on the RHS is the baroclinic torque, which is a result of misaligned pressure and density gradients. The last term on the RHS indicates how fast the vorticity changes as a result of viscous diffusion. It is significant to realize that the viscous diffusion term in high R_e has a much smaller effect on the vorticity transport than the other three terms because the inertia force is more dominant away from the wall. The numerical and experimental studies show that the shedding vapor has a strong vortex-cavitation interaction, with vortex stretching and dilatation being the primary mechanism of cloud transition from 2D to the 3D cloud. As the shedding vapor cloud collapses downstream, the attached cavity shrinks quickly, changing from 3D to 2D. During this process, the attached sheet cavity and the boundary layer become very thin. The strength of the vortex stretching term and dilatation term decreases significantly with the extent of the cavitation region. Even though the baroclinic torque term has a smaller magnitude than the vortex stretching and dilatation terms, it is very important for the production of vorticity and modifies the vorticity field in regions with high density and pressure gradients, such as near the cavity closure and along with the liquid-vapor interface. Despite the fact that it is an unrelated issue for this project, it is critical to comprehend the 3D effect in hydrofoils and how this effect is reflected in the results when comparing numerical 2D with experimental results.

1.12 Main Effect of Cavitation in Hydraulics Performance

Several consequences of cavitation can be expected as:

- Drops in hydraulics system performance, for example, decreases in lift and drag increases of the foil, decreases in turbomachinery efficiency, lower ability to evacuate water in spillways, energy dissipation, and so on.
- It contributes to the production of noise and vibration which damages the structures,
- Wall erosion when the bubble gets extruded between the fluid and solid surface the solid surface is eroded. This effect acts like a creep and it reduces the machine's usable lifetime.

Chapter 2

Theoretical Formulation

2.1 Governing Equations

The basic governing equations of single-phase flow, i.e mass, momentum conservation are given below. The energy equation is neglected because the change in flow properties is taking place in the isothermal condition. From the single-phase flow conservation equation, we will extract the equations for the multiphase flow based on the assumption stated in [2, 7].

2.1.1 Homogeneous bubbly flows

From homogeneous nucleation theory [10] the microbubbles whose diameter is smaller than 0.5mm only are considered so that hydrostatic pressure can be neglected in comparison with surface tension. When the concentration of the bubbles in the flow exceeds these values the bubble will have a significant effect on the fluid dynamics of the suspending liquid. Then the analyses of the multiphase mixture will become too complex. In the large context of practical multiphase flows, one can find a wide range of homogeneities i.e. consisting of one phase that is very finely dispersed with the other phase of two-phase flow with a separate stream. The two asymptotic states are commonly referred to homogeneous and separated flows. They are often called homogenous mixture flows in the computational domain. The important aspect of this kind of flow is defining the relative motion between the two phases because two streams will move with different velocities and such relative motion between two phases is an implicit part of the study of separated flow. But based on the assumption that as two-phase flows are sufficiently well mixed and the disperse particle size is sufficiently small so as to eliminate any significant relative motion. Then the term homogeneous flow can be used to denote a flow with the relative motion to be zero. Many bubbly flows will come close to this approximation. In the absence of relative motion the governing mass and momentum conservation equations reduce to a form similar to those for single phase flow. It is possible to establish barotropic relation which controls the condensation and vaporization and this allows one to anticipate that entire spectrum of phenomena observed in single-phase flow dynamics.

2.1.2 Governing equations

The dynamic model of cavitation is established by using mixture continuity and momentum equations of RANS turbulence model as stated below[18].

$$\frac{\partial \rho_m}{\partial t} + \frac{\partial \rho_m u_j}{\partial x_j} = 0 \quad (2.1)$$

$$\frac{\partial \rho_m}{\partial t} + \frac{\partial \rho_m u_j}{\partial x_j} = \frac{\partial}{\partial x_j} \left[\mu_m \left(\frac{\partial u_i}{\partial x_j} + \frac{\partial u_j}{\partial x_i} \right) \right] - \frac{\partial}{\partial x_i} \left(P + \frac{2}{3} \mu_m \frac{\partial u_k}{\partial x_k} \right) + \rho_m g_i + \frac{\partial R_{ij}}{\partial x_j} \quad (2.2)$$

$$R_{ij} = -\rho \overline{u_i' u_j'} = -\frac{2}{3} \left(\rho k + \mu_t \frac{\partial u_l}{\partial x_l} \right) \delta_{ij} + \mu_t \left(\frac{\partial u_i}{\partial x_j} + \frac{\partial u_j}{\partial x_i} \right) + \tilde{R}_{ij} \quad (2.3)$$

The vapour fraction α is used to find density ρ and dynamic viscosity μ as shown in the equation below.

$$\alpha = \frac{\forall V}{\forall} \quad (2.4)$$

The mixture density and the viscosity are defined as follows:

$$\rho_m = \rho_l \alpha_l + \rho_v (1 - \alpha_l) \quad (2.5)$$

$$\mu_m = \mu_l \alpha_l + \mu_v (1 - \alpha_l) \quad (2.6)$$

The volume fraction transport equation is given by:

$$\frac{\partial \alpha_l}{\partial t} + \frac{\partial}{\partial x_j} (\alpha_l u_j) = \frac{\dot{m}}{\rho_l} \quad (2.7)$$

$$\dot{m} = \alpha_l \dot{m}^- + (1 - \alpha_l) \dot{m}^+ \quad (2.8)$$

$$\frac{\partial u_j}{\partial x_j} = \dot{m} \left(\frac{1}{\rho_l} - \frac{1}{\rho_v} \right) \quad (2.9)$$

In the above equations, ρ_l and ρ_v are the liquid and vapor density, respectively; α_l and α_v are the liquid fraction and the vapor fraction, respectively; μ_m is the mixture laminar viscosity and μ_t is the turbulent viscosity; and \dot{m}^+ and \dot{m}^- represent the condensation and evaporation rates, respectively.

2.2 Basic bubble dynamic equation

The liquid motion induced by a spherical cavity in an infinite medium under the uniform pressure at infinity seems to have been first considered by Besant in 1859. It was solved for inviscid liquid by Rayleigh in 1917, to explain the phenomenon of cavitation erosion. In 1948, Cole use the model of a spherical bubble containing a non-condensable gas. Plesset in 1954, consider the general case of bubble evolution for a viscous and non-compressible flow. In simple bubble dynamic model[10], we consider the dynamic evolution of the spherical bubble with a fixed center, that undergoes uniform pressure variation at infinity. This simple model demonstrates many practical cases such as bubble collapse, bubble formation from the nucleus, bubble oscillation, etc. This model is even suitable for more complicated situations, involving the motion of the bubble center.

2.2.1 Assumptions

The main assumption are the following:

- the liquid is incompressible and either Newtonian or inviscid;
- gravity is neglected;
- mass of the air inside the bubble is constant, its inertia is neglected. The transformation from one radius to another by the bubble take place in isothermal condition;
- the bubble is saturated with vapor when the local pressure of the liquid is well below the vapor pressure.

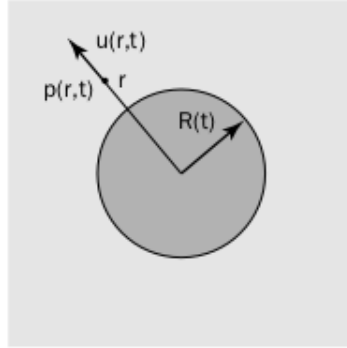


Figure 2.1: Rayleigh Plesset:Evolution of spherical bubble [10]

The functions to be determined, in the liquid domain $r \geq R(t)$, are the velocity $u(r,t)$ and the pressure $p(r,t)$ induced by the evolution of bubble as shown in (fig2.1).

2.2.2 Boundary and intial condition

In this derivation, we disregard the mass transfer through the interface, so $u(R,t)$ represents the liquid velocity at the interface as the interface velocity $\dot{R} = dR/dt$. For a viscous fluid of kinematic viscosity m , the normal stress at the surface is:

$$t_{rr}(R, t) = -P(R, t) + 2\mu \frac{\partial u}{\partial r} \Big|_{r=R} \quad (2.10)$$

The balance normal force is given by:

$$-t_{rr}(R, t) = P_v + P_g(t) - \frac{2S}{R} \quad (2.11)$$

where P_g stands for the partial pressure of the gas inside the bubble. With adiabatic gas transformation, the instantaneous gas pressure is related to the initial gas pressure P_{g0} using the following expression:

$$P_g(t) = P_{g0} \left[\frac{R_0}{R(t)} \right]^{3\gamma} \quad (2.12)$$

where γ is the ratio of heat gas capacities C_{pg} and C_{vg} . Thus, the pressure on the cavity interface is given by:

$$P(R, t) = P_v + P_{g0} \left[\frac{R_0}{R(t)} \right]^{3\gamma} - \frac{2R}{R} + 2\mu \frac{\partial u}{\partial r} \Big|_{r=R} \quad (2.13)$$

Consider the liquid far from the bubble at rest so that $u(\infty, t) \rightarrow 0$ and the pressure $P(\infty, t)$ also denoted $P_\infty(t)$, is assumed given. For the initial condition denoted by the subscript 0, the bubble is assumed to be in thermodynamic equilibrium, i.e., $\dot{R}(0)$.

$$P_{\infty 0} = P_{g0} + P_v - \frac{2S}{R_0} \quad (2.14)$$

2.2.3 Rayleigh-Plesset eqaution

Based on spherical symmetry, the flow is irrotational and is of the source type (or sink type). The mass consevation of an incompressible fluid is given by $\nabla \cdot \vec{u} = 0$ that gives:

$$u(r, t) = \dot{R} \frac{R^2}{r^2} \quad (2.15)$$

The viscous term of the Navier-Stokes equation is zero in this specific case. Thus for both a viscous and non-viscous fluid, the momentum equation is:

$$\frac{\partial u}{\partial t} + u \frac{\partial u}{\partial r} = - \frac{1}{\rho} \frac{\partial p}{\partial r} \quad (2.16)$$

By taking equation(2.15) in to account, it follows:

$$\ddot{R} \frac{R^2}{r^2} + 2\dot{R}^2 \left[\frac{R}{r^2} - \frac{R^4}{r^5} \right] = - \frac{1}{\rho} \frac{\partial p}{\partial r} \quad (2.17)$$

By integrating with respect to r and by considering the condition at infinity, one obtains:

$$\frac{P(r, t) - P_\infty(t)}{\rho} = \ddot{R} \frac{R^2}{r^2} + 2\dot{R}^2 \left[\frac{R}{r} - \frac{R^4}{4r^4} \right] \quad (2.18)$$

This equation is similar to Bernoulli's equation for a variable unsteady flow of inviscid liquid. On the other hand, when substituting $r=R$, equation(2.18) gives:

$$\frac{P(r, t) - P_\infty(t)}{\rho} = R\ddot{R} + \frac{3}{2}\dot{R}^2 \quad (2.19)$$

Finally, from the equation(2.13) for the pressure at the interface, and noting that:

$$\frac{\partial u}{\partial r} \Big|_{r=R} = - \frac{2\dot{R}}{R} \quad (2.20)$$

equation(2.19) becomes:

$$\rho \left[R\ddot{R} + \frac{3}{2}\dot{R}^2 \right] = P_v - P_\infty(t) + P_{g0} \left(\frac{R_0}{R} \right)^{3\gamma} - \frac{2S}{R} - 4\mu \frac{\dot{R}}{R} \quad (2.21)$$

This equation is called the Rayleigh-Plesset equation, which permits us to determine the temporal evolution of the radius R and simultaneously the pressure field in the liquid when the law P_∞ is given. For inviscid liquid, the last term on the right-hand side vanishes. The corresponding equation is known as the Rayleigh equation. Both the Rayleigh-Plesset equation and Rayleigh equation are differential and enormously non-linear, because of the inertial terms. With the use of the Rayleigh equation, we can solve the problem of bubble collapse and bubble explosion. In most instances, the inertial forces are dominant and viscosity no longer plays a huge role. The position of surface tension is often a secondary case of bubble collapse.

2.2.4 Schnerr-Sauer mass transfer model

According to the detailed literature review, the cavitation model used in this study was developed by Schneer and Sauer. The Schneer and Sauer mass transfer cavitation model are derived from a simplified Rayleigh-Plesset equation which neglects the second-order derivative of the bubble radius. In reference[18, 7], the vapor fraction was related to the average radius of the gas nucleus and number density. The condensation and evaporation rates are as follows:

$$\alpha_v = \frac{n_0 \frac{4}{3} \pi R^3}{\left(n_0 \frac{4}{3} \pi R^3 + 1 \right)} \quad (2.22)$$

$$\dot{m}^+ = C_v \frac{\rho_v \rho_l}{\rho} \alpha_v (1 - \alpha_v) \frac{3}{R} \sqrt{\frac{2(P_v - P)}{3\rho_l}} \quad (\text{if } P < P_v) \quad (2.23)$$

$$\dot{m}^- = C_c \frac{\rho_v \rho_l}{\rho} \alpha_v (1 - \alpha_v) \frac{3}{R} \sqrt{\frac{2(P - P_v)}{3\rho_l}} \quad (\text{if } P > P_v) \quad (2.24)$$

where m^+ , m^- are the condensation and evaporation rate respectively; C_v , C_c are the empirical coefficient for condensation and evaporation, with the value 2, 1 respectively.

The bubble radius can be related to the vapor volume fraction and the bubble number density:

$$R = \left(\frac{\alpha_v}{1 - \alpha_v} \frac{3}{4\pi n_0} \right) \quad (2.25)$$

From the equation of radius the parameter n_0 is the number of gas nucleus per unit volume. This is an important parameter and it set as 1.6×10^{13} in the phaseChangeProperties of constant folder in OpenFOAM.

2.3 Introduction to Turbulence

The majority of flows in engineering application encounters turbulence[9]. Therefore appropriate turbulent models should be essential when dealing with complex turbulence flow problems. The main properties of turbulent flows are:

- High unsteadiness,
- Three-dimensionality,
- High diffusivity(turbulent diffusion),
- Dissipation,
- Coherent structure,
- Fluctuations on broad ranges of length and time scales.

2.3.1 Reynolds-average Navier-Stokes equation

In Reynolds averaging, the solution variables in the instantaneous Navier-Stokes equations are decomposed into a mean and fluctuating parts; referred from[15, 9]:

$$u_i = \bar{u}_i + u_i' \quad (2.26)$$

where \bar{u}_i , u_i' are the mean and fluctuating velocity components. For pressure and other scalar quantities:

$$\phi = \bar{\phi} + \phi' \quad (2.27)$$

where ϕ denotes scalar quantities such as pressure, energy, or species concentration. By substituting expression of this form for the flow variables into the instantaneous continuity and momentum equations and by taking an ensemble average, the ensemble-averaged momentum equations is written in cartesian tensor form in the following way:

$$\frac{\partial \rho}{\partial t} + \frac{\partial}{\partial x_i}(\rho u_i) = 0 \quad (2.28)$$

The ensemble-average momemtum equation is:

$$\frac{\partial}{\partial t}(\rho u_i) + \frac{\partial}{\partial x_j}(\rho u_i u_j) = -\frac{\partial P}{\partial x_i} + \frac{\partial}{\partial x_j} \left[\mu \left(\frac{\partial u_i}{\partial x_j} + \frac{\partial u_j}{\partial x_i} - \frac{2}{3} \delta_{ij} \frac{\partial u_l}{\partial x_l} \right) \right] + \frac{\partial}{\partial x_j} \left(-\rho \bar{u}_i' u_j' \right) \quad (2.29)$$

Equation(2.28) and Equation(2.29) are called Reynolds-average Navier-Stokes (RANS) equations. They resemble Navier-Stokes equation. The only the difference is that the velocities and other scalars quantities are expressed as ensemble-averaged values. An additional term that is present in the RANS equation represents the effect of turbulence. This term $(-\rho \bar{u}_i' u_j')$ is called Reynolds stresses. This must be modeled to overcome the closure problem(the number of unknown variables is inconsistent with the number of the equations). Different types of turbulence modeling are being used to model this Reynolds stress term which is an additional term in the RANS ensemble-momentum equation.

2.3.2 k- ω sst turbulence model

After a detailed literature review, it is better to use the k- ω sst model for the 2D NACA0012 hydrofoil investigated in this thesis [18, 9]. The shear-stress transport(sst) k- ω model was developed by Menter to effectively blend the robust and accurate formulation of the k- ω model in the near-wall region with the freestream independence of the k- ϵ model in the far-field. The sst k- ω model is similar to the standard k- ω model but includes the following refinements.

- The standard k- ω model and the transformed k- ϵ model are both multiplied by a blending function and both models are added together. The blending function is designed to be one in the near-wall region, which activates the standard k- ω model and zero away from the surface, which activates the transformed k- ϵ model.
- The sst model incorporates a damped cross-diffusion derivative term in the ω equation.
- The definition of the turbulent viscosity is modified to account for the transport of the turbulent shear stress.
- The modeling constants are different.

These features make sst k- ω model more accurate and reliable for a wider class of flows such as adverse pressure gradient flows, airfoil, transonic shock waves, than standard k- ω model.

2.3.3 Transport equation for the sst k- ω model

Turbulent kinetic energy equation reads:

$$\frac{\partial \rho k}{\partial t} + \nabla \cdot (\rho k \bar{u}) - \nabla \cdot (\Gamma_{k,eff} \nabla k) = \min(G, c_1 \beta^* k \omega) - \beta^* k \omega \quad (2.30)$$

$$\Gamma_{k,eff} = \alpha_k \mu_t + \mu \quad (2.31)$$

Specific dissipation rate equation reads as:

$$\frac{\partial}{\partial t}(\rho \omega) + \nabla \cdot (\rho \omega \bar{u}) - \nabla \cdot (\Gamma_{\omega,eff}) = \gamma_{min} \left[S_2, \frac{c_1}{a_1} \beta^* \omega \max \left(a_1, \omega, b_1 F_2 \sqrt{S_2} \right) \right] - \beta \omega^2 + (1 - F_1) C D_{k\omega} \quad (2.32)$$

$$\Gamma_{\omega,eff} = \alpha_\omega \mu_t + \mu \quad (2.33)$$

The eddy viscosity is calculated as:

$$\mu_t = \frac{a_1 \rho k}{\max \left[a_1 \omega, b_1 F_2 \sqrt{2} \left| \frac{1}{2} \left(\nabla \bar{u} + (\nabla \bar{u})^T \right) \right| \right]} \quad (2.34)$$

and the production of turbulent kinetic energy reads:

$$G = \mu_t S_2 \quad (2.35)$$

$$S_2 = 2 \left| \frac{1}{2} \left(\nabla \bar{u} + (\nabla \bar{u})^T \right) \right|^2 \quad (2.36)$$

The use of $k-\epsilon$ in the freestream removes the sensitivity of the original $k-\omega$ to the inlet freestream turbulence properties. The use of $k-\omega$ in the inner parts of the boundary layer makes the model usable close to the wall without damping functions. Thus, each of the constant represents a blend of constants from $set_1(k-\omega)$ and $set_2(k-\epsilon)$:

$$\alpha_k = F_1(\alpha_{k1} - \alpha_{k2}) + \alpha_{k2} \quad (2.37)$$

$$\alpha_\omega = F_1(\alpha_{\omega1} - \alpha_{\omega2}) + \alpha_{\omega2} \quad (2.38)$$

$$\beta = F_1(\beta_1 - \beta_2) + \beta_2 \quad (2.39)$$

$$\gamma = F_1(\gamma_1 - \gamma_2) + \gamma_2 \quad (2.40)$$

where the blending is performed via blending functions, F_1 is a function that is one in the sublayer and logarithmic region of the boundary layer and gradually switches to zero in the wake region:

$$F_1 = \tanh \left[(\arg_1)^4 \right] \quad (2.41)$$

$$\arg_1 = \min \left(\min \left[\max \left(\frac{\sqrt{k}}{\beta^* \omega y}, \frac{500 \mu}{\rho y^2 \omega} \right), \frac{4 \alpha_{\omega2} \rho k}{C D_{k\omega} + y^2} \right], 10 \right) \quad (2.42)$$

F_2 is a function that is one for the bioundary-layer flows and zero for free shear layers:

$$F_2 = \tanh \left[(\arg_2)^2 \right] \quad (2.43)$$

$$\arg_2 = \min \left[\max \left(\frac{2\sqrt{k}}{\beta^* \omega y}, \frac{500\mu}{\rho y^2 \omega} \right), 100 \right] \quad (2.44)$$

positive term of cross-diffusion term is introduced for numerical stability:

$$CD_{k\omega+} = \max(CD_{k\omega}, 10^{-10}) \quad (2.45)$$

$$CD_{k\omega} = 2\rho\alpha_{\omega 2} \frac{\nabla k \cdot \nabla \omega}{\omega} \quad (2.46)$$

Closure coefficient have the following values: $\alpha_{k1} = 0.85$, $\alpha_{k2} = 1$, $\alpha_{\omega 1} = 0.5$, $\alpha_{\omega 2} = 0.856$, $\beta_1 = 0.075$, $\beta_2 = 0.0828$, $\beta^* = 0.09$, $\gamma_1 = 5/9$, $\gamma_2 = 0.44$, $a_1 = 0.31$, $b_1 = 1$, $c_1 = 10$.

2.3.4 Near-wall treatment

When examining a portion of the wall-bounded turbulent flows, the near-wall area is separated into the inner and outer turbulent boundary layers. The inner wall is briefly investigated because, all of the key phenomena for near-wall flow modeling in CFD occur in this layer. Various regions of the turbulent boundary layer are shown in(figure2.2)

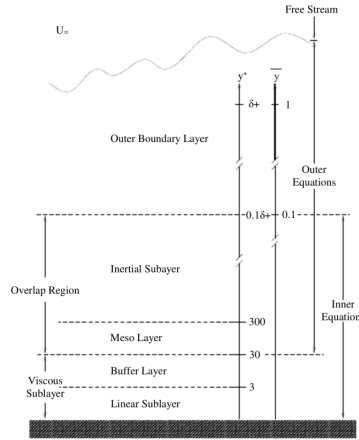


Figure 2.2: Regions of the turbulent boundary layer [14]

From the figure(2.2) the inner layer consists of: the viscous linear sublayer($0 < y^+ < 5$), the buffer sublayer($5 < y^+ < 30$) and the inertial sublayer($30 < y^+ < 200 - 300$) where y^+ is the normalised distance tot he wall calculated as:

$$y^+ = \frac{C_\mu^{1/4} k^{1/2}}{\nu} y \quad (2.47)$$

The molecular viscosity dominates the viscous sub-layer, and turbulence effects are minimal. The turbulent layer viscosity dominates the inertial sub-layer, making molecular viscosity irrelevant. Both turbulence and molecular viscosity are equally relevant in the buffer layer.

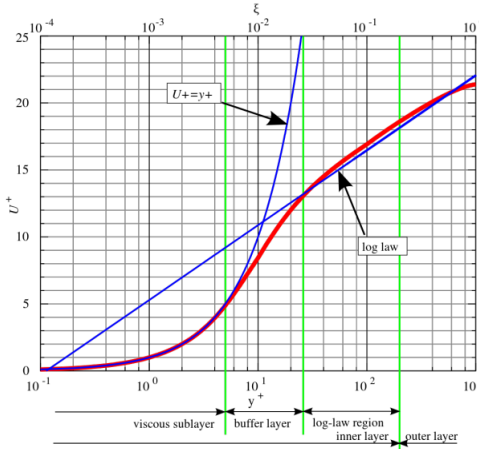


Figure 2.3: Law of the wall [14]

The assumptions described allow for the use of simple relations to represent the behavior of influencing variables in the near-wall region (as functions of wall distance). Figure(2.3) depicts the relationship between dimensionless velocity $U +$ and $y +$. (the red line represents the experimental observations and the two blue lines represent the two derived profiles). The experimental results were best suited by the linear profile in the viscous sublayer and the logarithmic profile in the inertial sublayer, with the buffer sublayer serving as a smooth transition between the two. As a result, the first cell center should be placed in either the viscous linear sublayer or the inertial sublayer. Because the buffer sublayer reflects a transition from linear to log, it should be avoided. Placing the first cell in the linear sublayer is assigned for low Reynolds turbulence modeling while placing in the inertial(log-layer) is a characteristic of high Reynolds turbulence modeling. In OpenFOAM wall function for the field k is denoted with $kQRWallFunction$, for field $\omega WallFunction$ and the correction μ_t is done in $\omega NutWallFunction$.

2.3.5 Automatic wall treatment for $k-\omega$ sst turbulence model

The equation has a known solution in both the viscous and inertial (log-layer) sublayers, the $k-\omega$ sst turbulence model does not require extra damping functions to behave as a low Reynolds model. Because the ω equation has a known solution in both viscous and inertial(log-layer) sublayer. Menter [14] devised a blending technique based on this feature that enables a smooth shift from high to low Reynolds formulation and vice versa. Despite the smooth shift, the buffer layer is not correctly represented by automatic wall treatment.

$$\omega = \sqrt{\omega_{vis}^2 + \omega_{log}^2} \quad (2.48)$$

where ω_{vis} and ω_{log} are defined as follows:

$$\omega_{vis} = \frac{6\mu}{\beta_1 \rho y^2} \quad (2.49)$$

$$\omega_{log} = \frac{k^{1/2}}{\kappa C_\mu^{1/4} y} \quad (2.50)$$

The value of ω for the cell adjacent to the wall is obtained from eqaution(2.48). In these cells the production term G is given by:

$$G = G_{vis} (if y^+ \leq y^+_{lam}) \quad (2.51)$$

$$G = G_{log}(if y^+ \geq y^+_{lam}) \quad (2.52)$$

$$G_{vis} = 0 \quad (2.53)$$

$$G_{log} = \frac{C^{1/4} \mu k^{1/2} (\mu_t + \mu) |\nabla \bar{u}|}{\kappa y \rho} \quad (2.54)$$

where

$$y^+_{lam} = \frac{\ln \left(\max \left(E y^+_{lam}, 1 \right) \right)}{\kappa} \quad (2.55)$$

where E is a dimensional constant with default value of 9.8 and y^+ from equation(2.47) are calculated.

Chapter 3

Case setup

3.1 A test case

With the help of the OpenFOAM tutorial case study, a test case was set up for the simulation of multiphase flow over a NACA0012 hydrofoil. The geometry is from a compressible flow tutorial where $k-\omega$ sst turbulence model was adopted. The *blockMeshDict* of that tutorial is relevant for the thesis since it helps to tune the mesh based on requirement. To set up the case folders for multiphase simulation, another case study tutorial was used: multiphase/interFoam/RAS/propeller. The mass transfer model used in the tutorial is Schnerr-Sauer, that relevant for thesis it was explained in (chapter 2 section 2.2.4) and also the tutorial assists with setting up the 3 folders to run the simulation properly. The essential file from the tutorials are copied in the working directory. files from the tutorials. The case setup of the working directory contains three folders *0/*, *constant/*, and *system/*, with slight modification in all three of them as outlined below.

3.2 Computational domain

The flow field around the hydrofoil is modeled in two-dimensional.

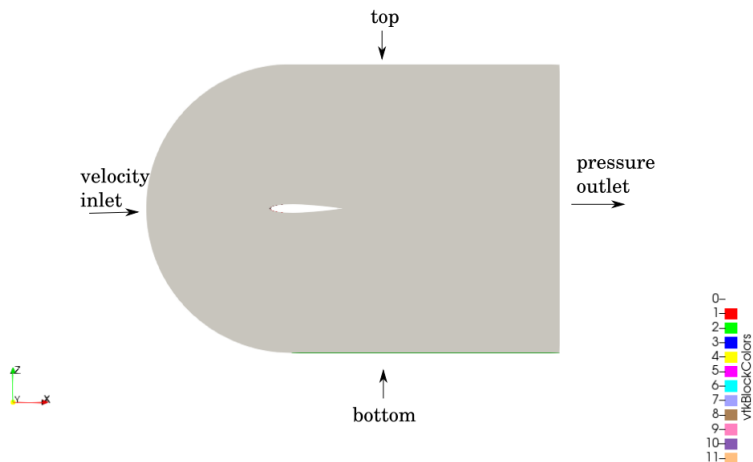


Figure 3.1: Schematic representation of flow field around 2D NACA0012 hydrofoil with boundary condition

The transformation from 2D to 3D performed in domain of *blockMeshDict* by adding ymax=0.45 and ymin=-0.45 which is in span wise direction.

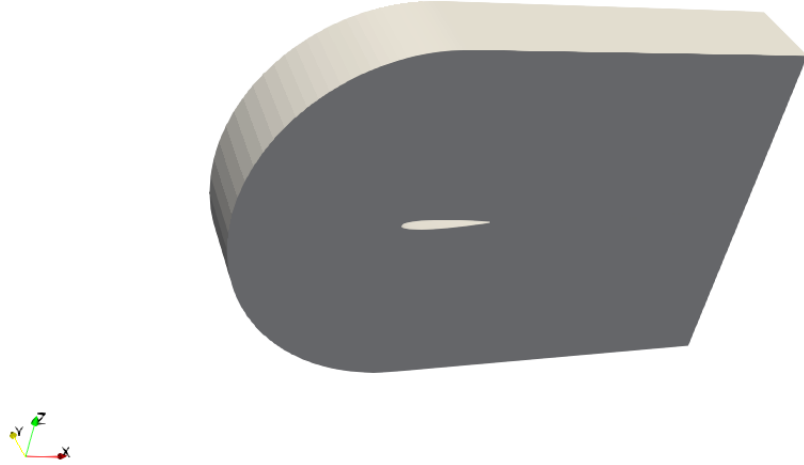


Figure 3.2: Schematic representation of flow field around 3D NACA0012 wing

3.2.1 Boundary and initial condition

The boundary condition and parameters of work condition are taken from the reference [18] which is stated below: The parameter of working condition is stated below:

hydrofoil	Wall
inlet	Velocity
outlet	Pressure
top and bottom	Symmetry

Table 3.1: Boundary condition

Velocity(U)	5 m/s
Cavitation number (σ)	0.8
Turbulence kinetic energy(k)	$0.0185 \text{ m}^2/\text{s}^2$
Specific dissipation rate(ω)	621.626 s^{-1}
pressure(P_v)	9358.6848 N/m^2
Reference pressure(P_{out})	$0.203\text{e}5 \text{ N/m}^2$
Chord length(C)	100 mm
Angle of attack(α)	3.2° to 8°

Table 3.2: parameters of work condition

3.3 Grid study

In this thesis, the influence of mesh size was discussed. Three types of mesh were analyzed to determine the appropriate mesh size for numerical simulation. It was clear that the force coefficient increased when mesh size was small. It can be seen from the verification and validation results that the value of numerical uncertainty is larger than the comparison error. Thus, the calculated results are in agreement, but there is not enough evidence to confirm their accuracy. The grid study is discussed in the table below, which takes the AOA 5° degree into account.

Grid no	No of cells	No of faces	No of points	C1	Cd
Grid A	16000	64240	32480	0.72	0.028
Grid B	21600	86690	43780	0.68	0.027
Grid C	38500	154390	77780	0.59	0.021

Table 3.3: Grid study of AOA 5°

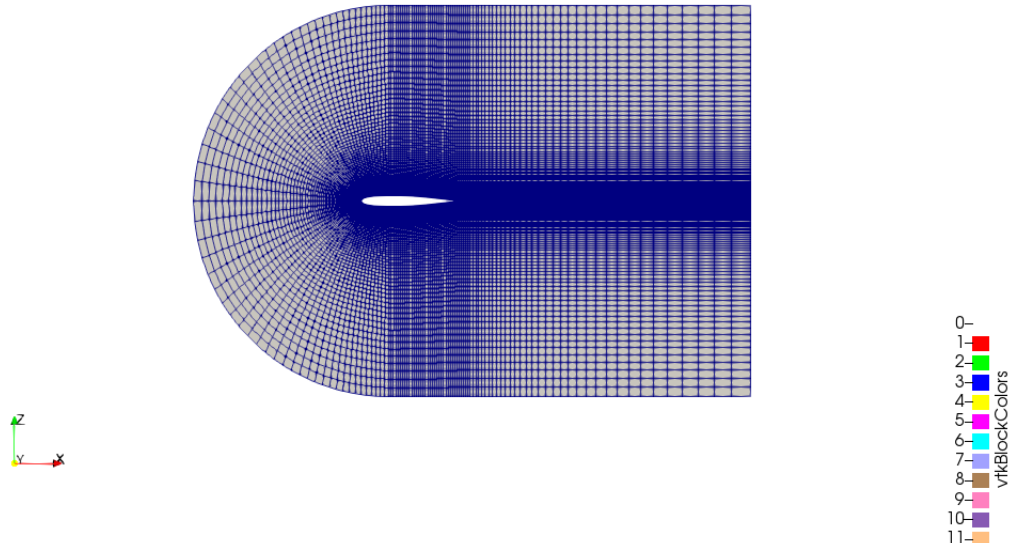


Figure 3.3: Grid lines in coarse mesh over view

3.4 Case folder setup

3.4.1 0 Folder

This folder contains the working parameters at the boundaries for the initial time step, such as velocity as $U/$ which is a reference velocity, $p_{\text{ref}}/$ reference pressure, $\omega/\$ specific dissipation rate, $k/\$ turbulence kinetic energy, $\nu/\$, $\alpha.\text{water}/$ vapour fraction respectively. In order to include the angle of attack of the hydrofoil with respect to the incoming flow it is better to specify the velocity as $V_x=V\cos\alpha$ and $V_z=V\sin\alpha$ (normal direction is in z direction). The internalField and boundaryField of each files in the 0/ folder are stated below:

PATCH	FIELD	UNITS	TYPE	VALUE
inlet	U	m/s	fixed value	5
	P	Pa	zero gradient	-
	ω	s^{-1}	fixed value	621.626
	k	m^2/s^2	fixed value	0.0185
	nut	m^2/s	zero gradient	0
	alpha.water	-	fixed value	1
outlet	U	m/s	zero gradient	-
	P	Pa	fixed value	0.203e5
	ω	1/s	fixed value	621.626
	k	m^2/s^2	fixed value	0.0185
	nut	m^2/s	fixed value	0
	alpha.water	-	fixed value	1

Table 3.4: Boundary condition

3.4.2 Constant folder

This folder includes 4 files namely *g/*, *momentumTransport/*, *phaseChangeProperties/*, *transportProperties/* and two other subfolders which are called *geometry* and *polyMesh*. In *geometry/*, the NACA0012.obj is present. This file which helps to run the *blockMesh* command in the working directory to generate the *polyMesh/* folder in the constant folder. This folder contains some files such as *boundary/*, *face/*, *neighbor/*, *owner/*, *points/*.

The *momentumTransport/* file is the place for the declaration of turbulence model.

momentumTransport		
simulationType	RAS	model: kOmegaSST

Table 3.5: Parameters in momentumTransport

PhaseChangeProperties		
phaseChangeModel	SchnerrSauer	SchnerrSauerCoeffs on
pSat(saturation vapor pressure)		9358.6848 N/m^2

Table 3.6: Parameters in phaseChangeProperties

The *phaseChangeProperties/* file is the place for the declaration of mass transfer model and saturation vapor pressure. The *transportProperties/* is the place to declare the phase of a mixture, its properties, as well as the cavitation number.

3.4.3 System folder

This folder contains files such as *blockMeshDict/*, *controlDict/*, *decomposeParDict/*, *extrudeMeshDict/*, *fvScheme/*, *fvSolution/*. Tune mesh based on requirements aids mesh grading in the *blockMeshDict/*. By specifying ymin=-0.45 and ymax=0.45 in the domain of *blockMeshDict/*, one can go from 2D to 3D.

Time step control

The courant number affects the reliability and stability of the unstable flow simulation. The maxCo should be set around 5 in the *controlDict/* file. Based on the mesh adopted deltaT of 1e-5 s is sufficient to satisfy the condition. Note that cavitating flow calculations should always be initiated from a flow

transportProperties	
phases	water vapour
pSat	9358.6848 N/m^2
sigma(cavitation number)	0.8

Table 3.7: Parameters in transportProperties

field. When cavitation is toggled on, simulation must be restarted from the current flow field.

Discretisation schemes

In OpenFOAM, the free surface treatment does not account for turbulence. All free surface simulations can be viewed as direct numerical simulations (DNS). Therefore there is a high requirement for the mesh resolution of the interface. The solver uses the multidimensional universal limiter for explicit solutions (MULES) to maintain the boundedness of the phase fraction, regardless of the underlying numerical scheme, mesh structure, etc. The choice of schemes for convection is therefore not restricted to those that are strongly stable or bounded, e.g. upwind differencing.

Solution and algorithm control

The *fvSolution/* file controls the equation solvers, tolerances and algorithms. In the first subdictionary, solver, each linear-solver used for each discretized equation is specified. This is achieved by specifying the solver of each variable being solved, in this case: pcorr (pressure corrector), p_rgh, p_rghFinal (the final value of pressure after the correction), $(U|k|\omega)$, $(U|k|\omega)Final$ and alpha.water. The variable name is followed by the solver name and a dictionary containing the parameters that the solver uses. The pressure variables are solved with the aid of solver GAMG and smoother DICGaussSeidel(Diagonal Incomplete Cholesky), velocity and turbulence quantities are solved using a smoothSolver and smoother symGaussSeidel, and volume fraction alpha.water by way of MULES. The tolerance, and ratio of current to initial residuals, relTol, are specified afterward. The solver stops if one of the two tolerances falls beneath the targeted value. The precept of GAMG is to generate a quick solution on a mesh with a small number of cells, map this solution onto a finer mesh, and use it as an initial guess to obtain a correct solution on the fine mesh.

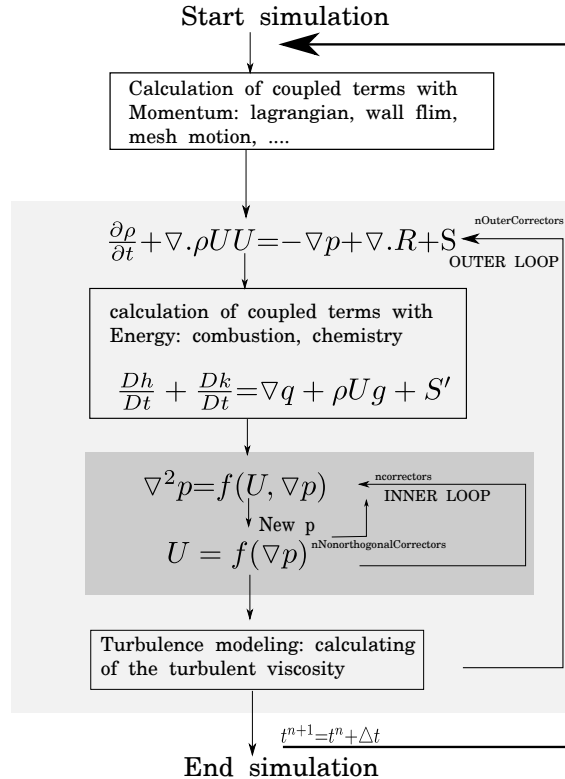


Figure 3.4: rhoPimpleFoam-based solvers

In OpenFOAM, any compressible flow solver is usually based on PIMPLE, which is an algorithm of iterative procedures for solving equations for velocity and pressure of unsteady problems. PIMPLE is an unsteady, transient SIMPLE. The number of correctors is specified by the keyword nCorrectors which should be greater than 1. The number of non-orthogonal correctors is specified by the nNonOrthogonalCorrectors keyword to account for mesh non-orthogonality which should be greater than 1. In the thesis, nOuterCorrectors should be set to 3, nCorrectors to 1, and nNonOrthogonalCorrectors to 0.

3.4.4 Postprocessing

To validate the force in the x and z direction it is better to use the force function object. This forces function object generates hydrodynamic force and moment data for surfaces. The forces comprise normal pressure and tangential viscous contributions. The forces obtained from the postprocessing are used for calculating the Cl and Cd. The basic operation of the forces function object is cited in *controlDict/* which comprises mandatory entries stated below:

forces1	
type	forces
libs	libforces.so
patches	hydrofoil(wall)

Table 3.8: Forces function object

Inorder to validate the term yplus the yPlus function object is used to computes the near wall y^+ for turbulence models by using yPlus functions sub-dictionary in *system/controlDict/*. It is better to use #includeFunc yPlus in the function of *controlDict/*. The pressure function object provides to validate

the total pressure coefficient. The following mandatory entries are included in the function of *controlDict*/ are stated below:

pressure1	
type	pressure
libs	libfieldFunctionObjects.so
mode	totalCoeff

Table 3.9: Pressure function object

Chapter 4

Result discussion

The main advantage of CFD analysis is its ability to calculate all flow parameters at every grid point in the domain studied, allowing for a very detailed description of the flow. The present study can be classified into two main parts: firstly, the non-cavitating flow and cavitating flow over the proposed NACA0012 hydrofoil are analyzed and secondly, the modeling and computations of unsteady cavitation shedding using the k- ω sst turbulence model are investigated. In this study, Cl and Cd are validated for a fixed cavitation number with different $\sigma/2\alpha$ which ranges from 2.86 to 7. The range was chosen because as stated in reference [18], the k- ω sst model is subjected to accuracy limitations for higher angles of attack. The lift and drag coefficient are computed as follows:

$$C_L = \frac{L}{\frac{1}{2}\rho_\infty U^2 \infty S_{ref}} \quad (4.1)$$

$$C_D = \frac{D}{\frac{1}{2}\rho_\infty U^2 \infty S_{ref}} \quad (4.2)$$

where $q = \frac{1}{2}\rho_\infty U^2 \infty S_{ref} = 1875 \text{ N}$.

The corresponding pressure coefficient is calculated by:

$$C_p = \frac{P - P_\infty}{\frac{1}{2}\rho_\infty U^2 \infty} \quad (4.3)$$

4.1 Non cavitating steady flow

The computational duration was 1 s long to ensure that the cavitation flow was fully developed. Firstly, the non-cavitating steady flow was calculated to verify the performance of the grid. The unsteadiness was not triggered in the range of $\sigma/2\alpha$ between 6 to 7 for those $\sigma/2\alpha$ values, the angle of attack α ranges from 3.2° to 3.8° . The condition which triggers cavitation did not present in this range which means the local pressure was not well below the vapor pressure. The flow is attached to the wall and the detailed information of the flow field from the NACA0012 wet flow simulation calculated by OpenFOAM is reliable when compared to the experimental results available in the given range. Because of the steady flow, it is fine enough to show the result with the final time step which is shown below:

As can be seen from the figure(4.1 and 4.2), there is a low-pressure area on the suction side of the hydrofoil and a high-pressure area on the pressure side. There is a progressive increase in the local velocity with a decrease in local pressure over the suction side of the hydrofoil as the increase of angle of attack.

$\frac{\sigma}{2\alpha}$ (radians)	α (degree)
2.86	8
3	7.6
3.5	6.5
4	5.7
4.5	5.0
5	4.5
5.5	4.1
6	3.8
6.5	3.5
7	3.2

Table 4.1: $\frac{\sigma}{2\alpha}$ and its corresponding α

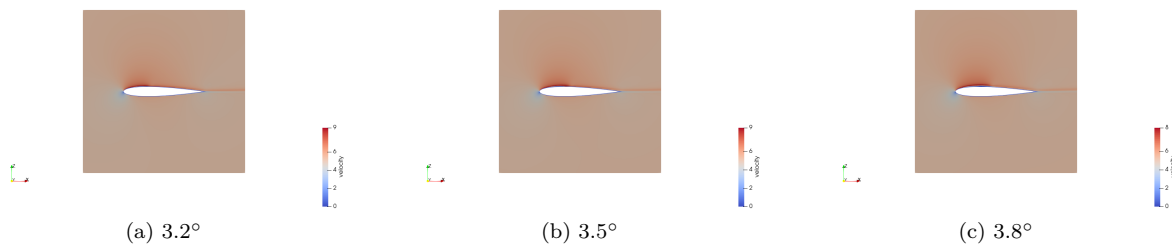


Figure 4.1: Change in velocity over a NACA0012, non cavitating flow

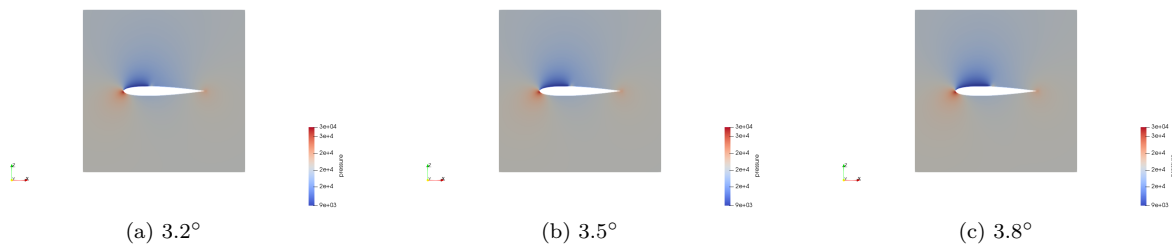


Figure 4.2: Change in pressure over a NACA0012, non cavitating flow

The graph of C_P versus x/c in the figure(4.5) shows that C_p remains constant for various angles of attack throughout a short range of x/c . The main cause is related to the fact that the change in alpha.water is extremely close to the leading edge of the suction side, as well as the pressure attaining saturated vapor pressure on the suction. After a certain distance, there is a steep rise in C_p , causing cavitation to vanish and a steady flow to be achieved. The point at which C_p rises on the suction side appears to vary for different angles of attack, as seen in the figure(4.5). The lift and drag coefficients are statistically averaged as seen in figure(4.6).

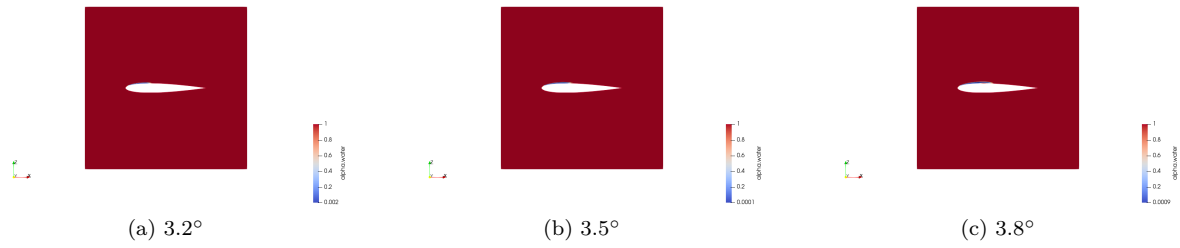


Figure 4.3: alpha.water variation over a NACA0012, non cavitating flow

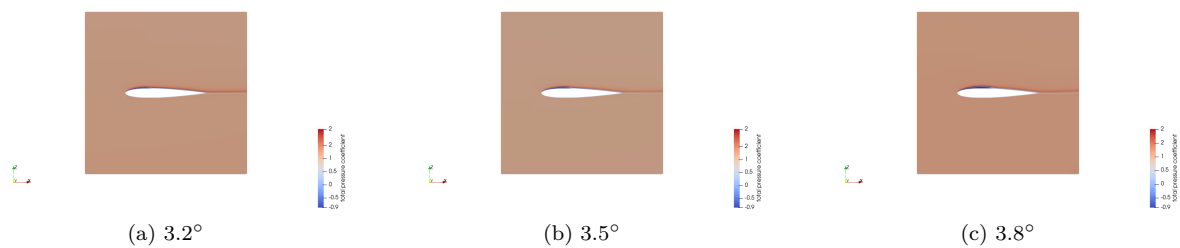


Figure 4.4: Change in pressure coefficient over a NACA0012, non cavitating flow

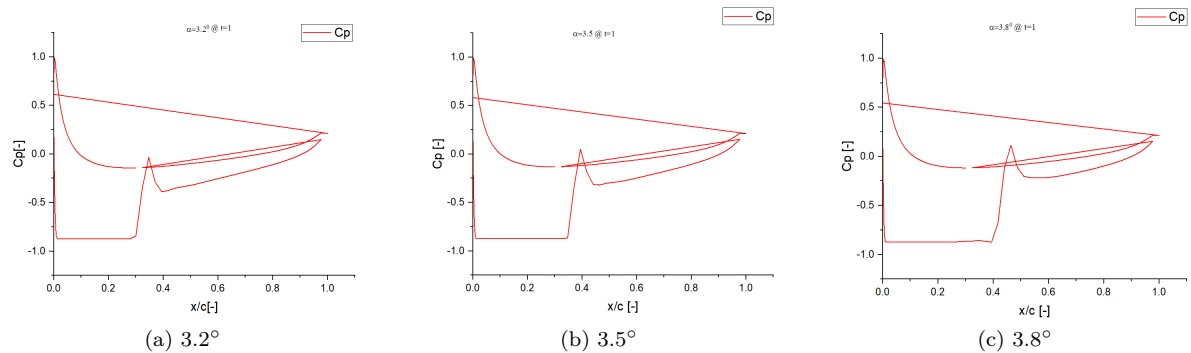


Figure 4.5: C_p vs x/c for a NACA0012 for non-cavitation flow

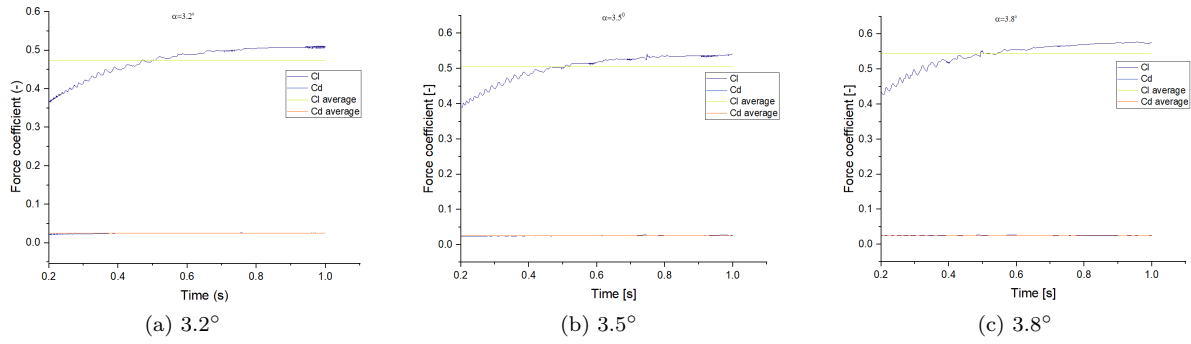


Figure 4.6: Variation of lift and drag coefficient with time on NACA0012, non cavitating flow

4.2 Cavitation unsteady flow

Re-entrant jet without shedding: AOA 4.1° to AOA 5.0° : A description of cavitation physics and the conditions for closed-type partial cavitation appears in chapter 1, along with discussions of re-entrant jet phenomena. As long as we keep all such conditions in mind, we can observe that, initially, tiny voids and droplets of small thickness were produced at the head of the hydrofoil. During that time, the cavity was still attached to the surface of the hydrofoil. As time progresses, the attached cavity moves towards the hydrofoil's tail. The cavity's thickness gradually increased along the wing chord until it reached its maximum and experienced a re-entrant jet as can be seen from table (4.4). Hence, this re-entrant jet is due to the minimum pressure occurring inside the cavity itself, so the curvature of the streamlines around tends to be directed towards the cavity. The re-entrant jet is so energized then only it can cut the cavity interface. However, there was no shedding of an unsteady vapor cloud as shown in table (4.6). The cavity was divided into two parts. The first part was often attached to the leading edge of suction side of the hydrofoil and the region $(1/4)^{th}$ of the chord will be highly influenced by the re-entrant jet. After a while, when the re-entrant jet crosses the rear area and moves towards the leading edge, the rear area gets suddenly reattached to the surface due to turbulent reattachment.

Re-entrant jet with unsteady cloud shedding: AOA 5.7° to AOA 8° : A sheet cavity with purely filled vapor appeared at the front of the suction side of the hydrofoil. The thickness of the cavity increases gradually and starts moving downward. The end of the cavity was located at the tail of the hydrofoil. The front part close to the leading edge is attached to the surface and the tail part of the cavity fell off and moved downstream. As we can be seen from the table (4.6) and table (4.7), periodic shedding takes place after a regular interval of time once the cavity length and thickness of the cavity decrease. Because of the unbalanced flow field and development of the low-pressure zone, the sheet cavity was further expanded. This means once the thickness of the cavity reduces after a shedding the cavity grows again and reaches its maximum, then the re-entrant jet (as can be seen from the table (4.4) and table (4.5)) cut the cavity interface and moved towards the leading edge, and then cloud shedding takes place. As we closely observed the alpha.water table (4.6) it can be seen that once the cavity breaks near $(1/3)^{th}$ of the chord, turbulent reattachment occurs near the tail of the suction side of the hydrofoil. As time progresses the wake is filled with vapor, and separated vortices at the tail of the hydrofoil could be noted.

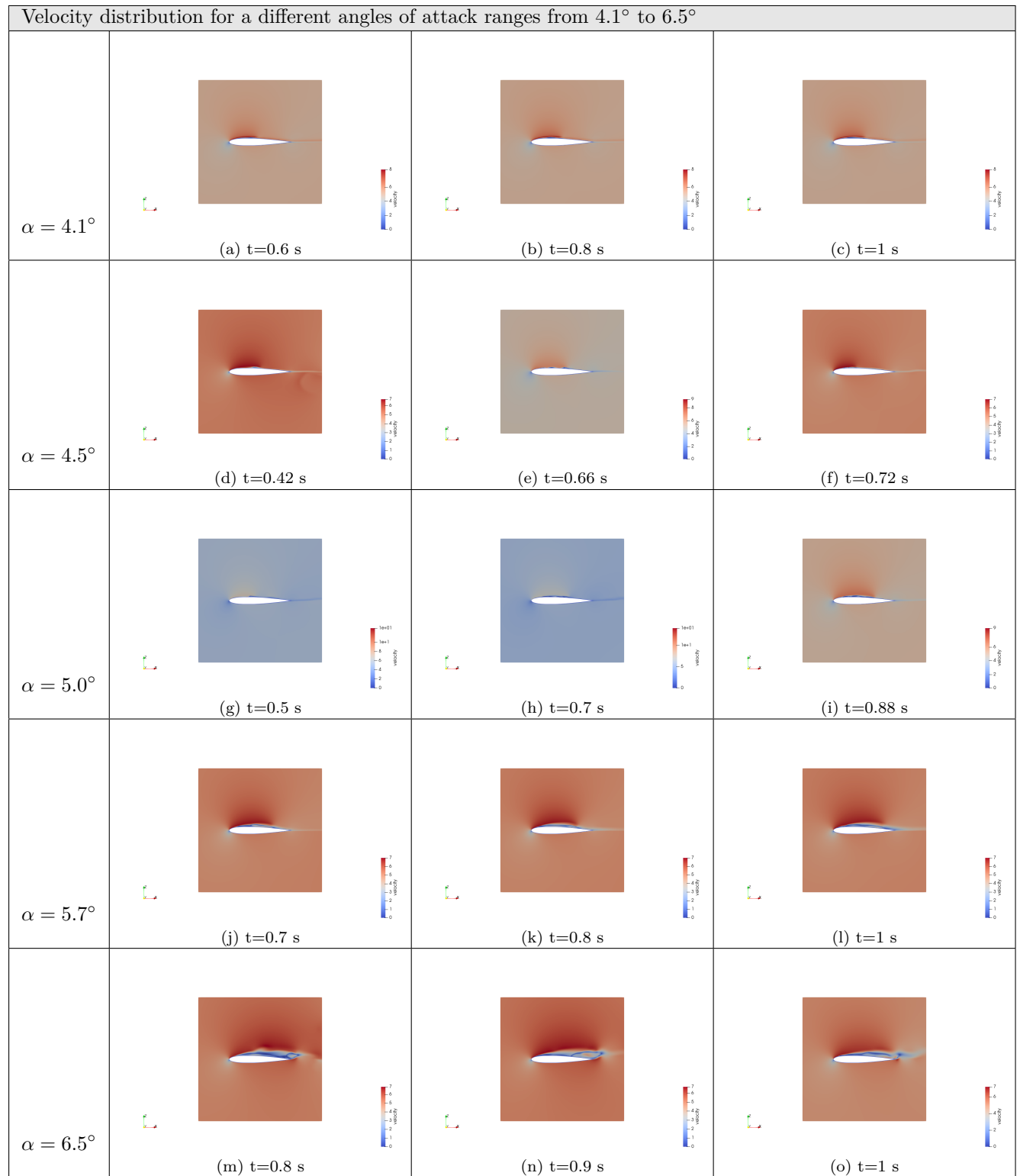


Table 4.2: Velocity distribution in a NACA0012 hydrofoil for an angles of attack ranges from 4.1° to 6.5° and different time period

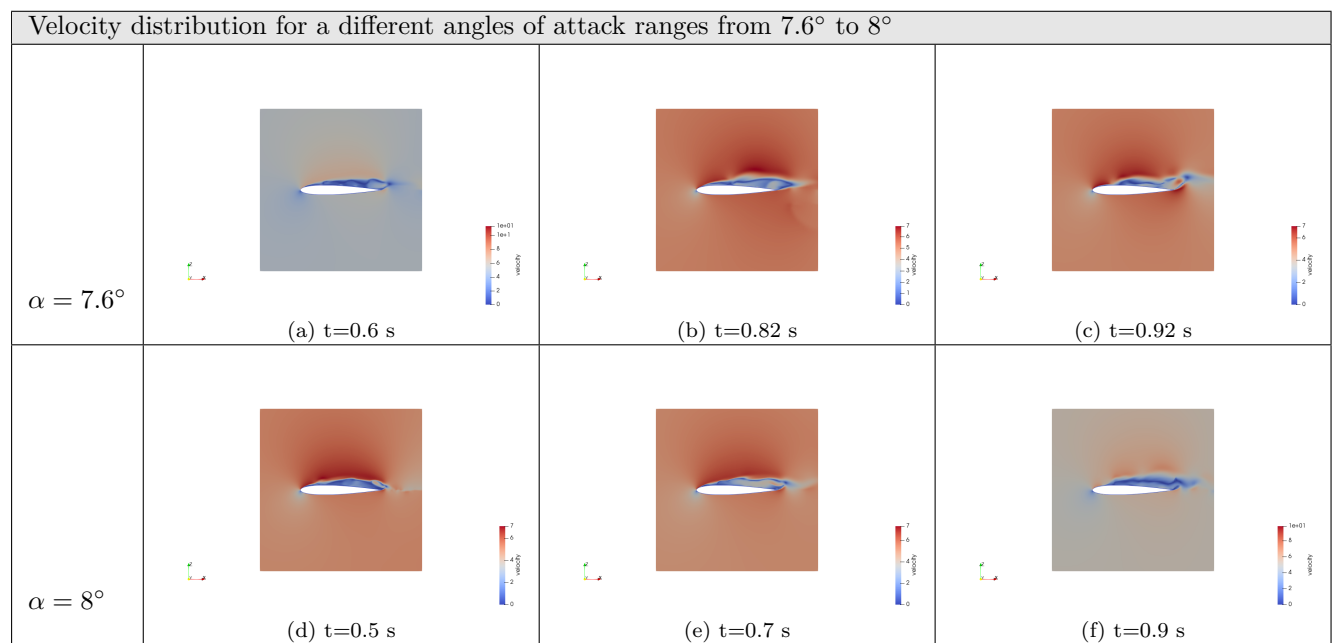


Table 4.3: Velocity distribution in a NACA0012 hydrofoil for an angles of attack ranges from 7.6° to 8° and different time period

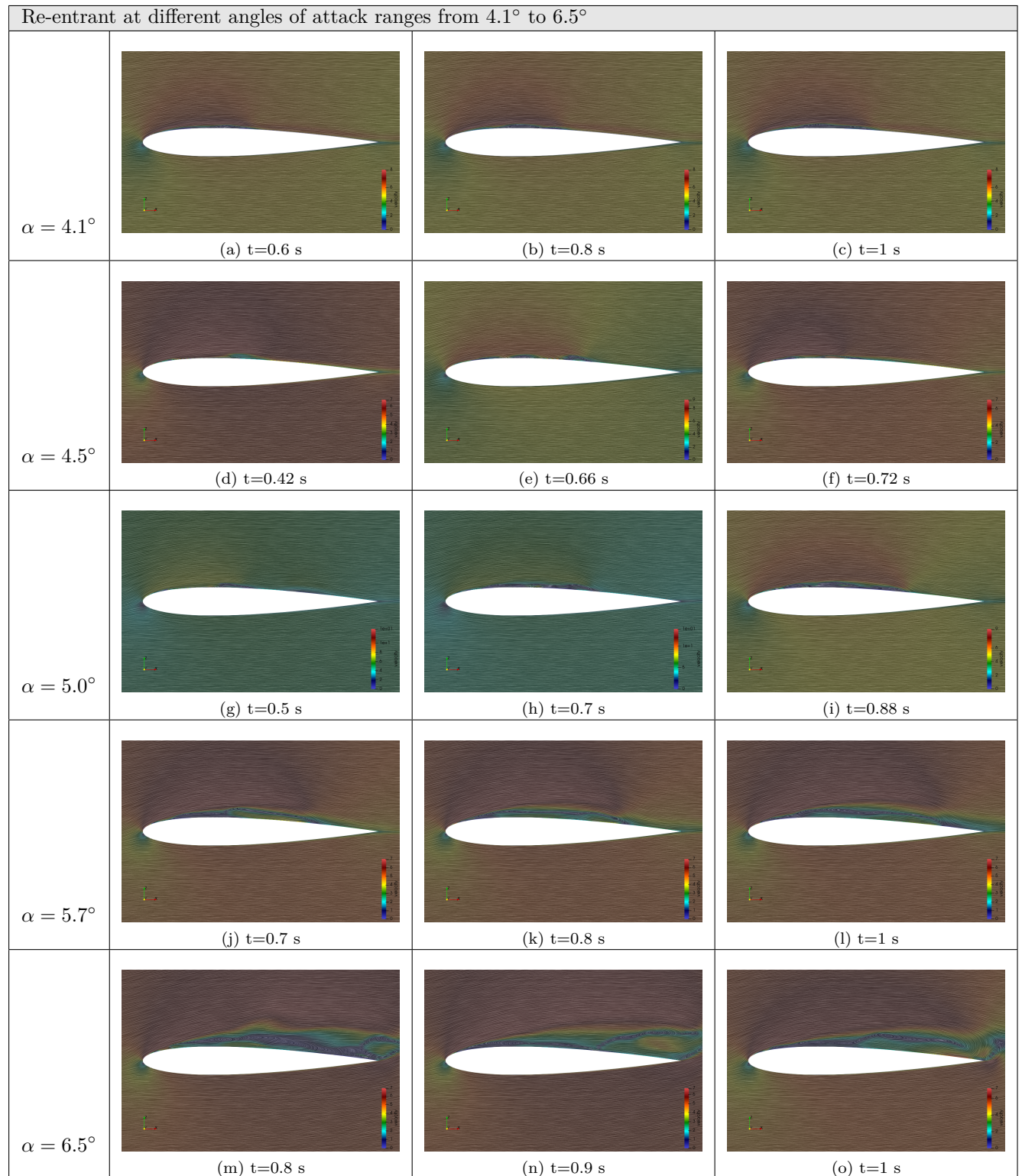


Table 4.4: Re-entrant jet over a NACA0012 hydrofoil at different angles of attack ranges from 4.1° to 6.5° and time period

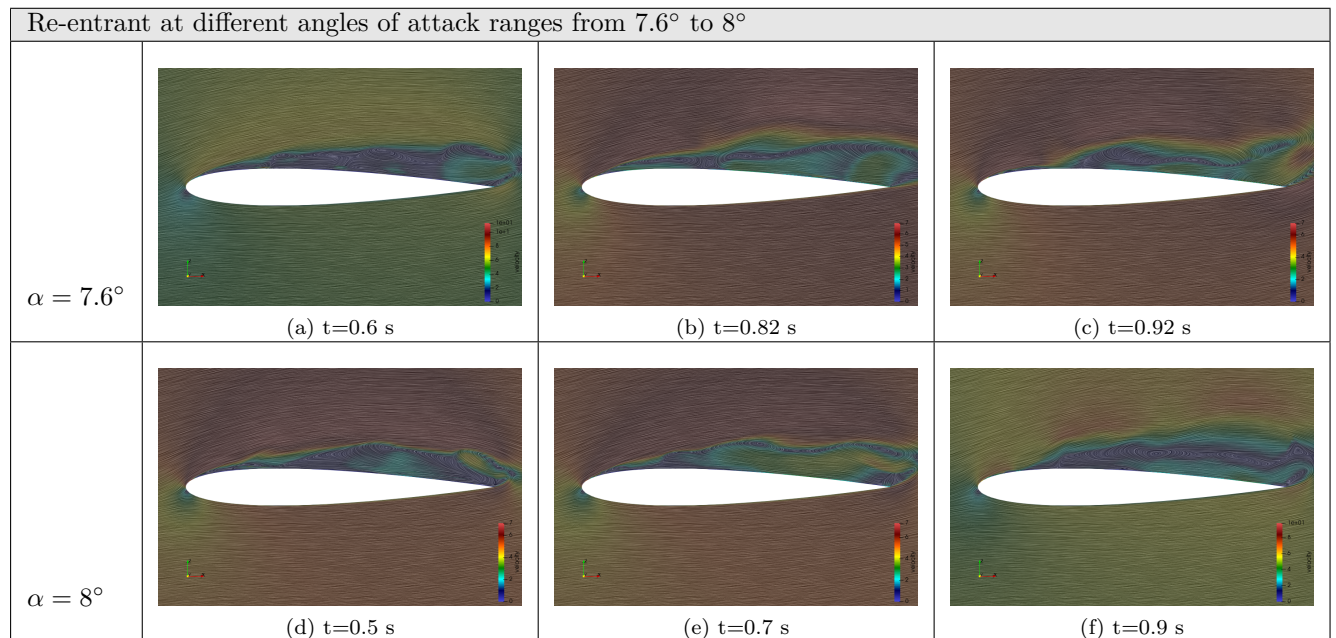


Table 4.5: Re-entrant jet over a NACA0012 hydrofoil at different angles of attack ranges from 7.6° to 8° and time period

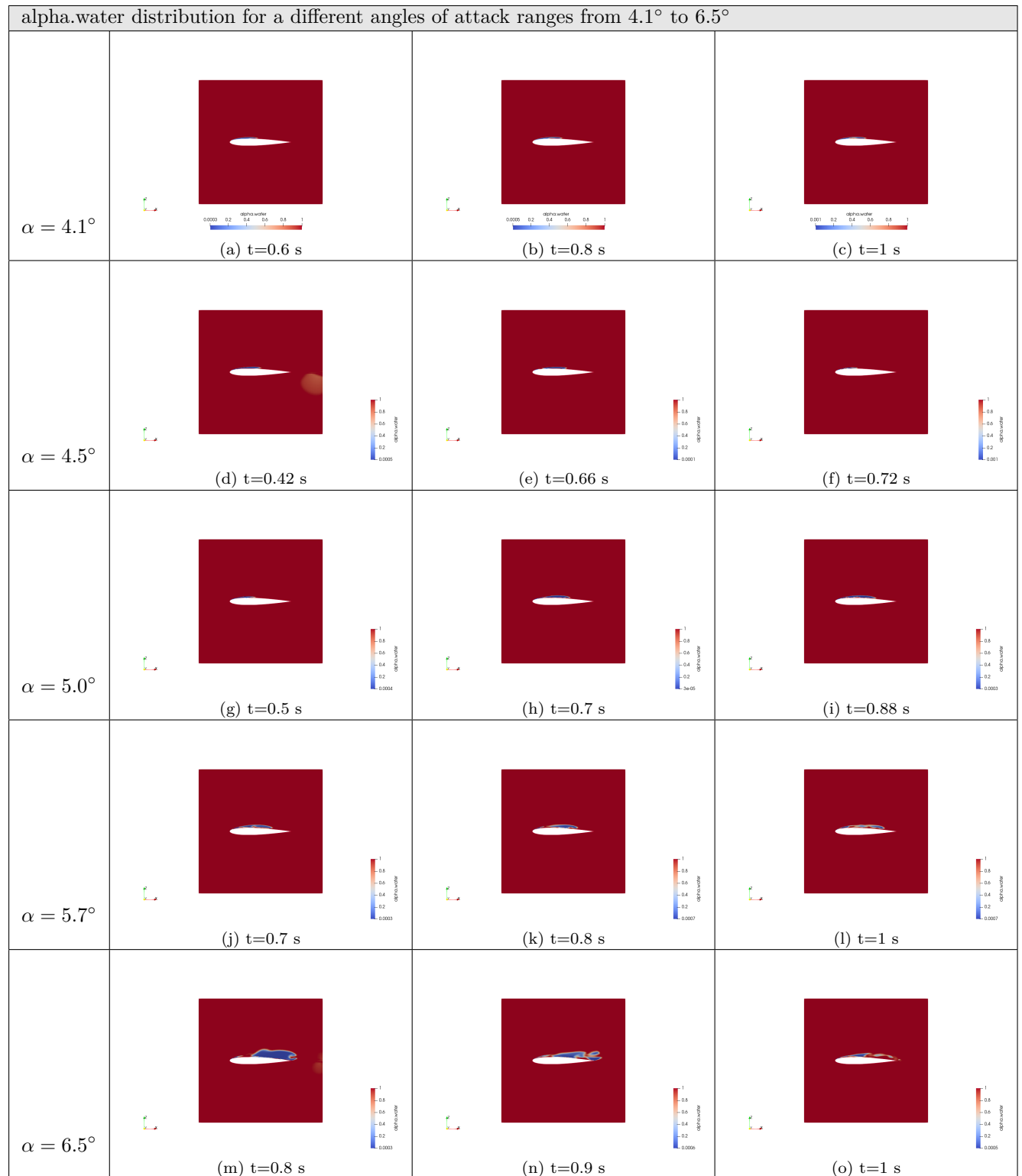


Table 4.6: alpha.water distribution over a NACA0012 hydrofoil at different angles of attack ranges from 4.1° to 6.5° and time period

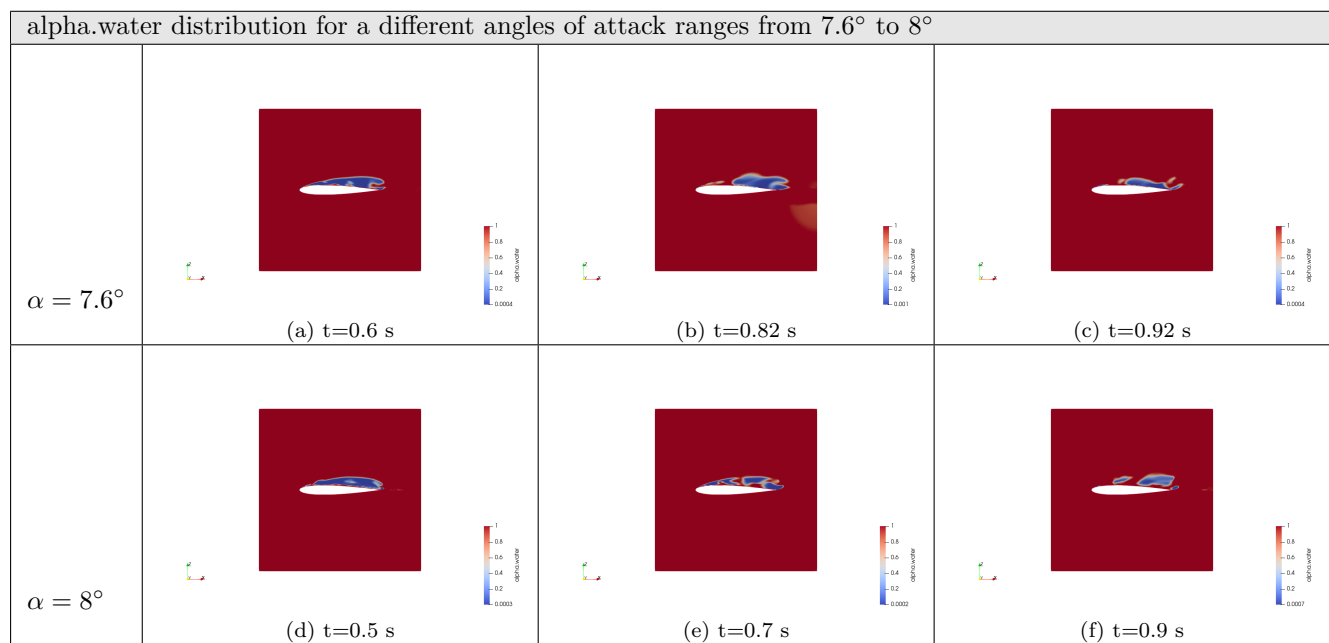


Table 4.7: alpha.water distribution over a NACA0012 hydrofoil at different angles of attack ranges from 7.6° to 8° and time period

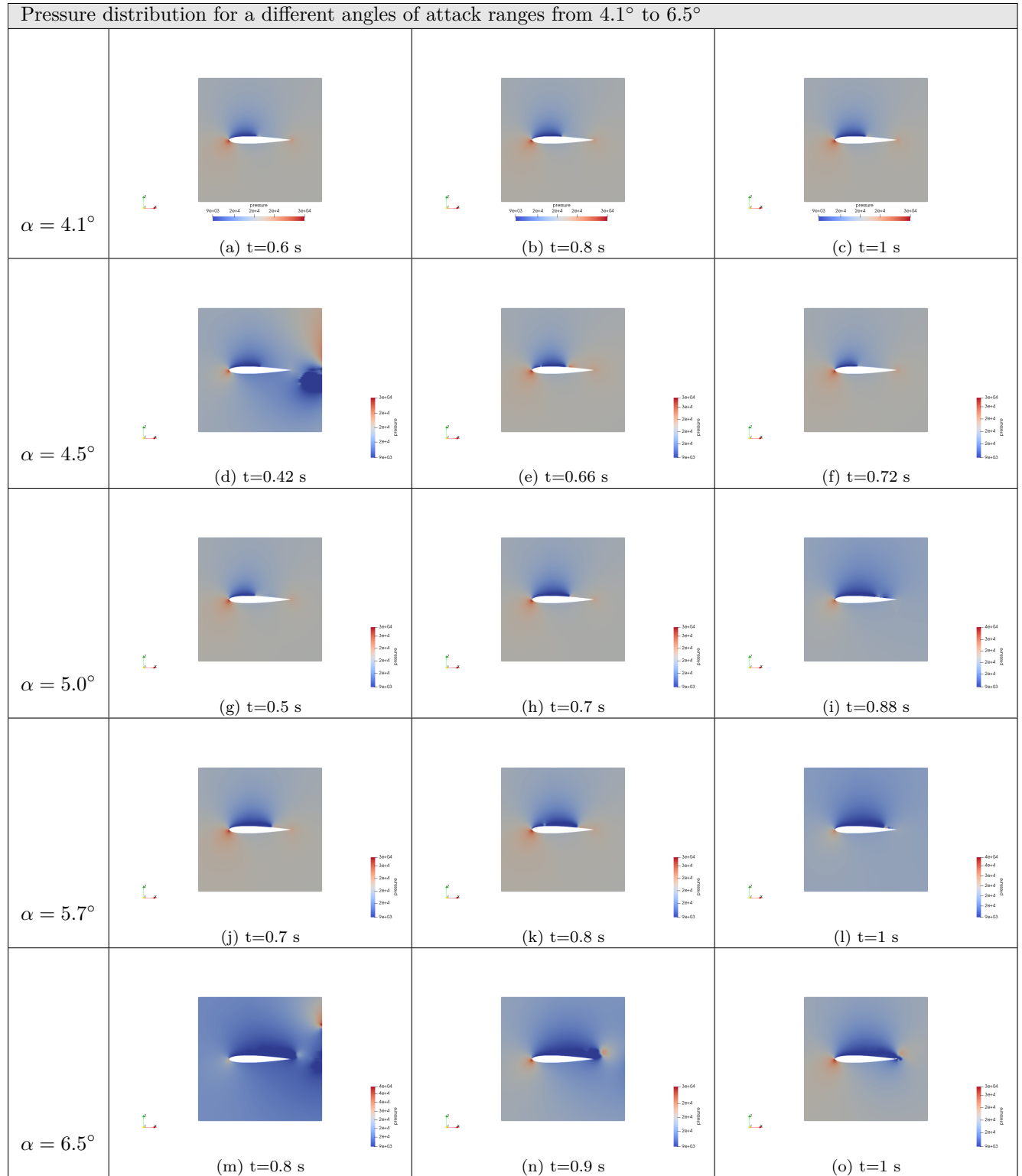


Table 4.8: Pressure distribution over a NACA0012 hydrofoil at different angles of attack ranges from 4.1° to 6.5° and time period

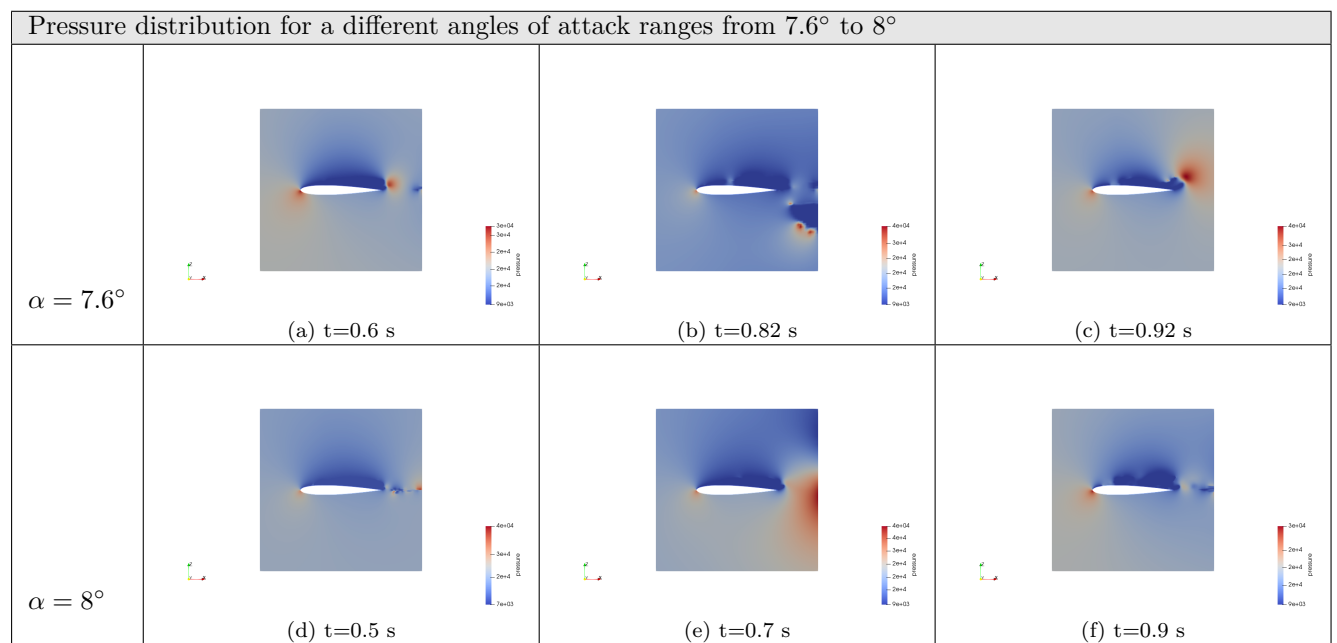


Table 4.9: Pressure distribution over a NACA0012 hydrofoil at different angles of attack ranges from 7.6° to 8° and time period

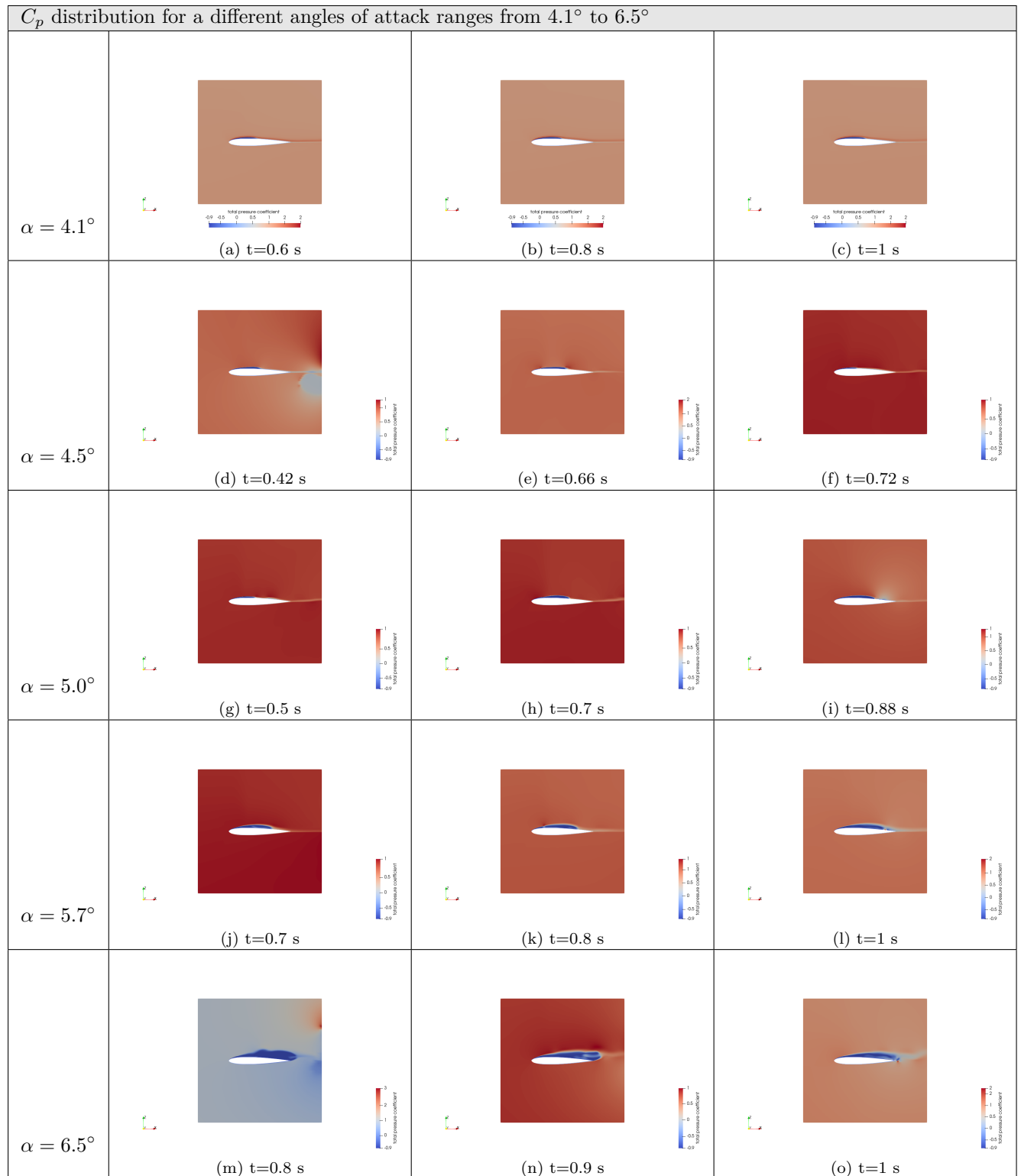


Table 4.10: C_p distribution over a NACA0012 hydrofoil at different angles of attack ranges from 4.1° to 6.5° and time period

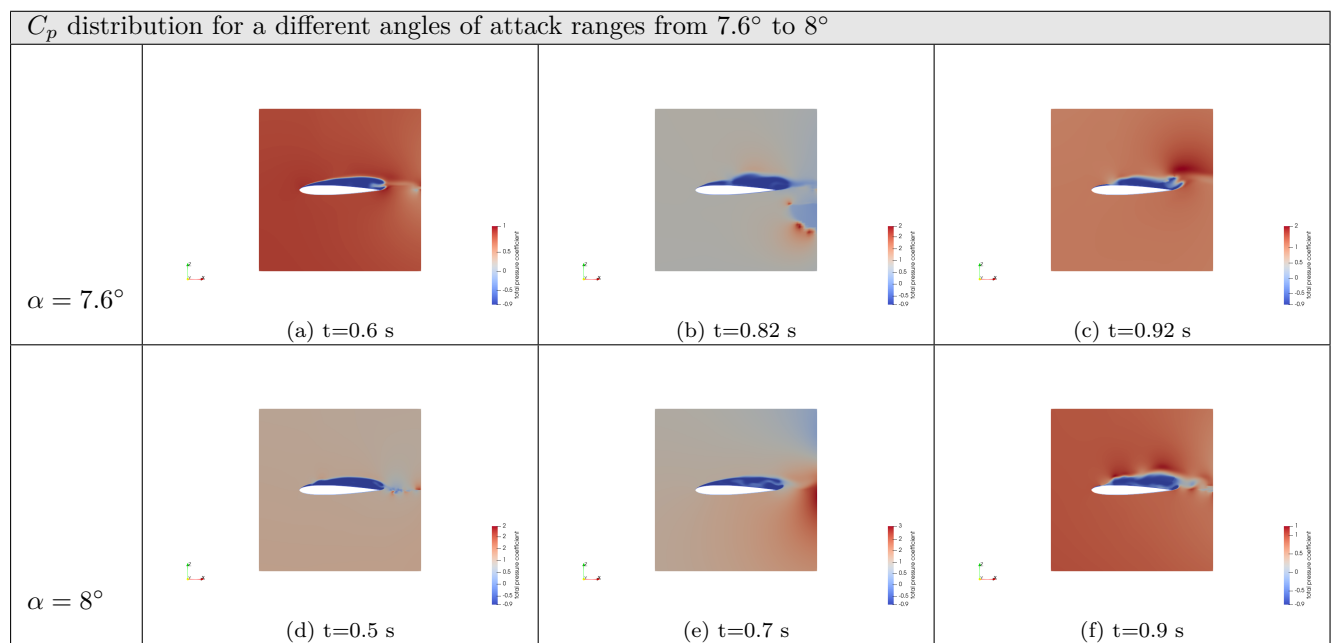
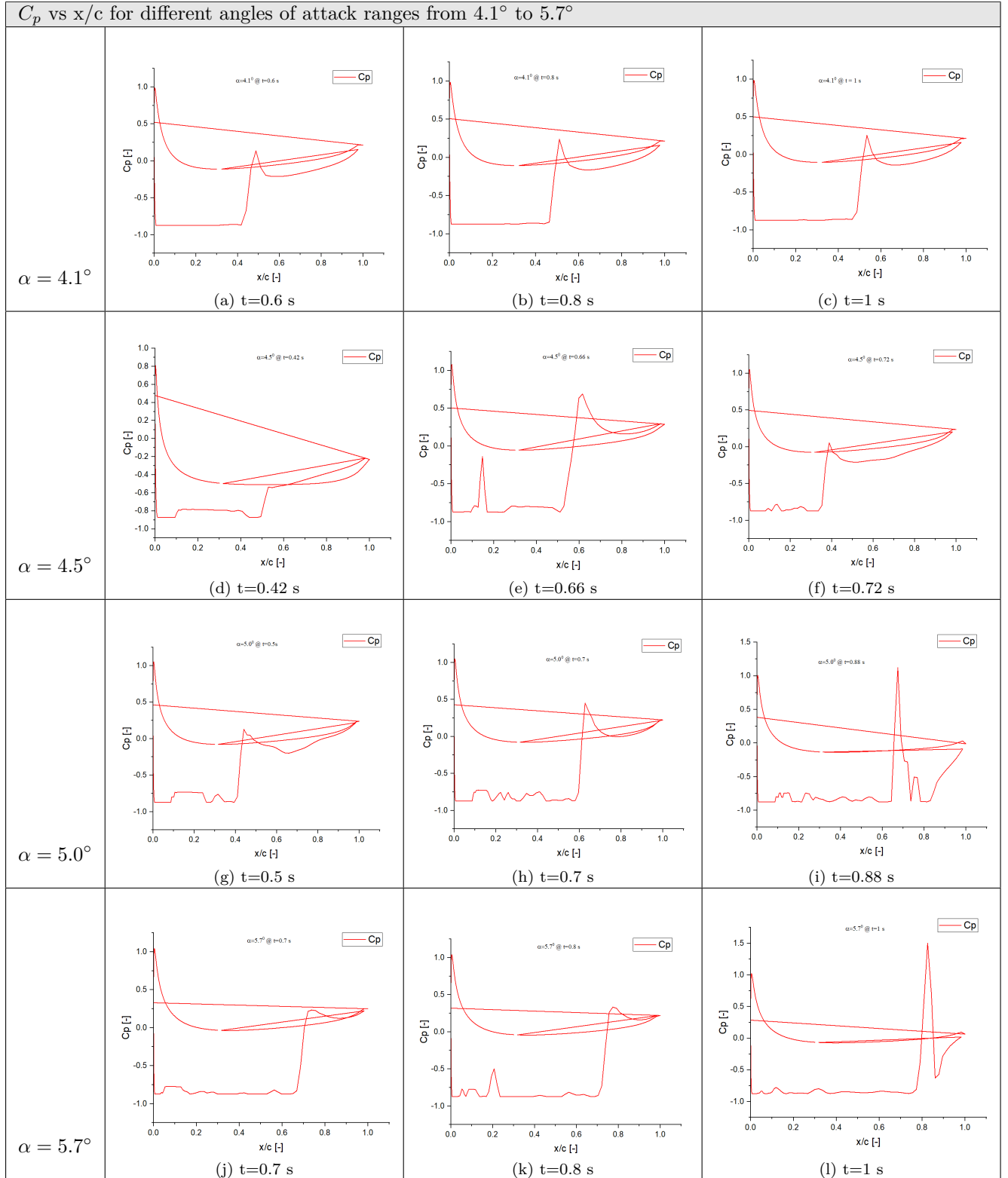
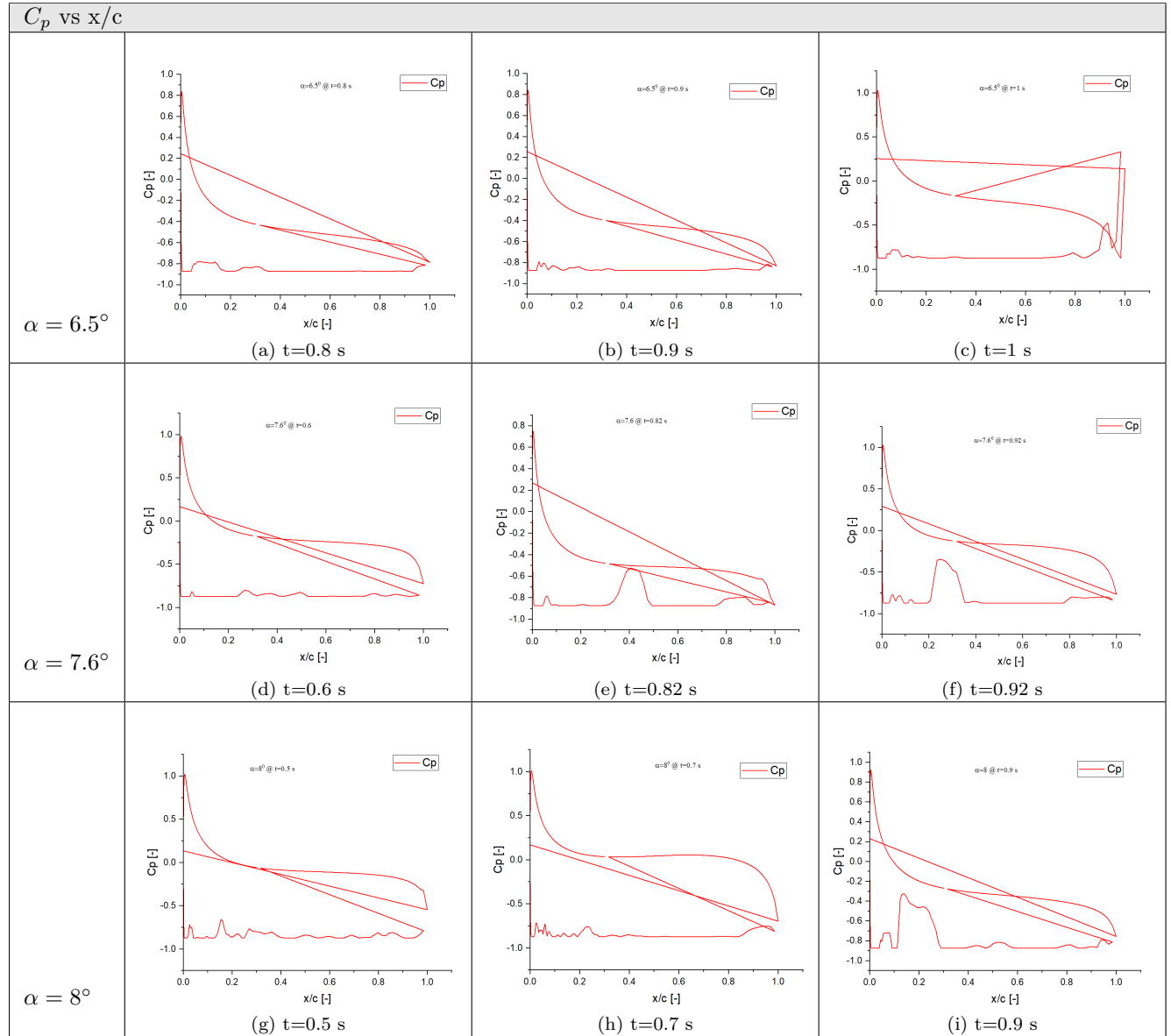


Table 4.11: C_p distribution over a NACA0012 hydrofoil at different angles of attack ranges from 7.6° to 8° and time period

Table 4.12: C_p vs x/c graph for different angles of attack ranges from 4.1° to 5.7° and time period

Table 4.13: C_p vs x/c graph for different angles of attack ranges from 6.5° to 8° and time period

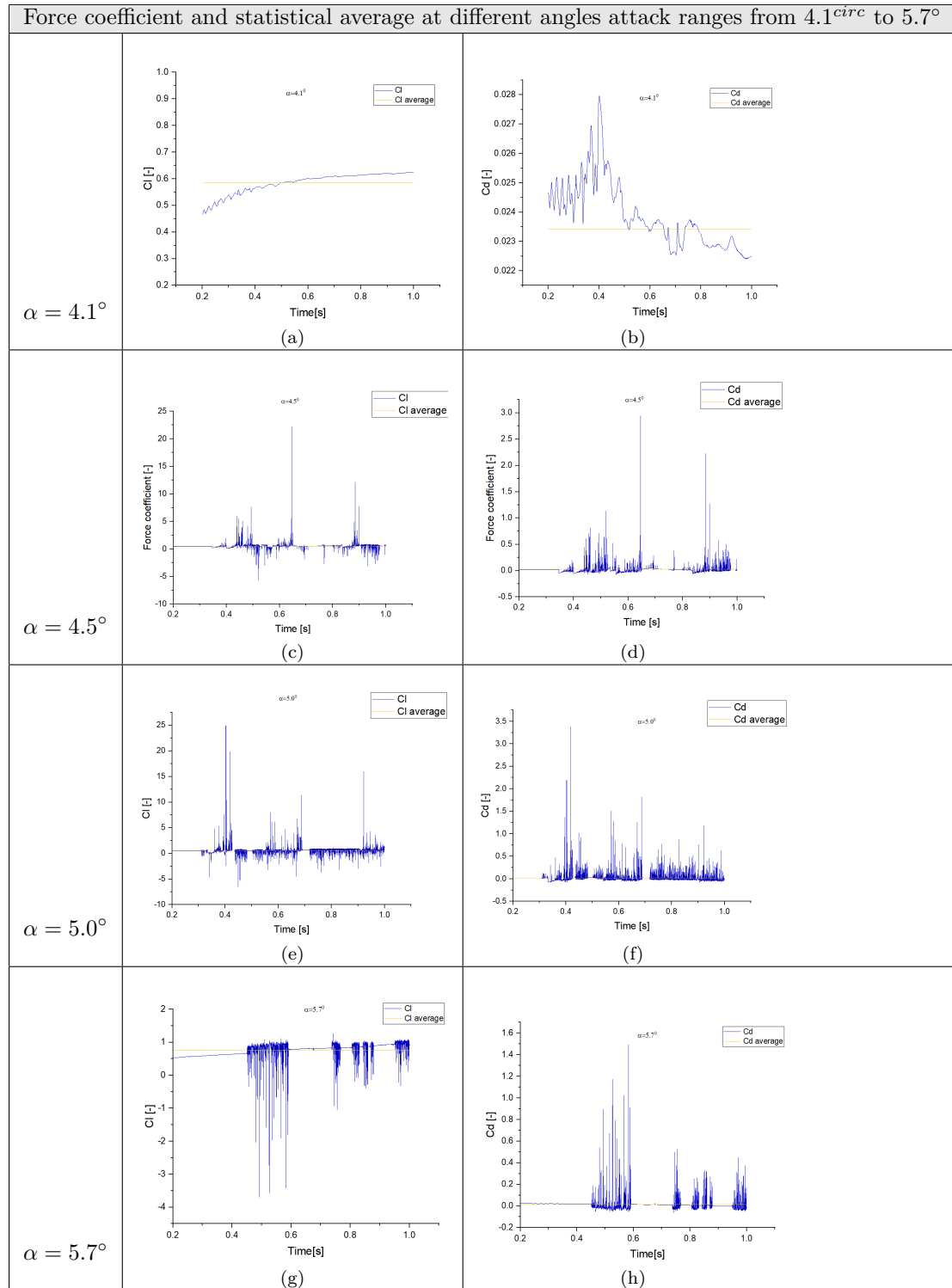


Table 4.14: Force coefficient at different angles of attack ranges from 4.1° to 5.7° over a NACA0012

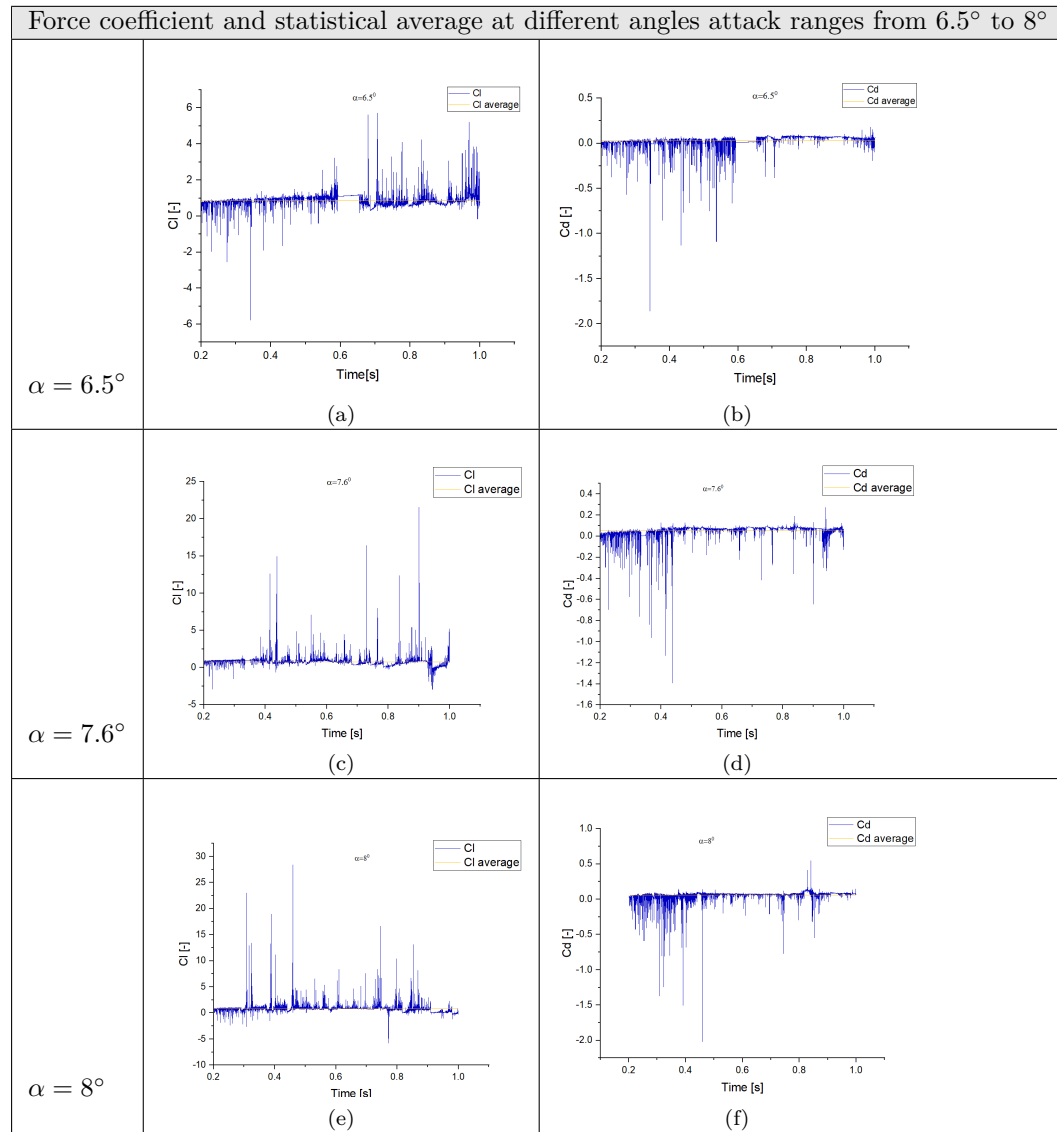


Table 4.15: Force coefficient at different angles of attack ranges from 6.5° to 8° over a NACA0012

Comparision of pressure between non-cavitating and cavitating flows over a suction side of hydrofoil: A better way to understand this concept is to compare the final time step of cavitation and non-cavitation flow. Figure(4.7) illustrates AOA 3.2° , which is a non-cavitating angle, in comparison to AOA 4.1° and 8° , which show a cavitating angle. During cavitation, the cavitation zone pressure was equal to the vapor pressure. As a result of the cavitation effect, the pressure distribution over the suction side of the membrane was greatly impacted, and the pressure gradient across the membrane cavity at the closure was greater than in the absence of cavitation. However, the change on the pressure side of the foil was much smaller. The other angles of attack in the table (4.8) and (4.9) show similar physics while comparing with the non-cavitating condition of pressure in figure(4.2). The change in pressure distribution also affected the overall hydrodynamic performance of the hydrofoil.

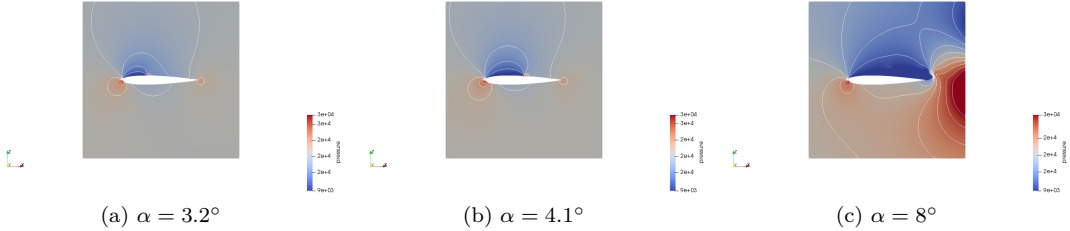


Figure 4.7: Contrast between the pressure distribution of the cavitating and non-cavitating flows

As can be seen in figure (4.5), the length of the cavity based on the cavitation zone is equal to the vapor pressure on the suction side of the hydrofoil which increases as the angles of attack increase as can be seen in the table (4.8) and (4.9). The C_p vs x/c graph in the table (4.12) and (4.13) illustrates this phenomenon. The graph shows that, for an AOA of 4.1° to 5.7° , there is a rise in pressure after $(1/4)^{th}$ of the chord of the suction side of the hydrofoil due to adverse pressure gradient. In AOA 6.5° to 8° , the length of the cavity is equal to the chord length of the hydrofoil. This means that the observed state completely covers the suction side of the hydrofoil with vapor. On the other hand, there is no pressure rise after $(1/4)^{th}$ chord and a transient state can be observed as can seen from the table(4.13). More often, these angles of attack are in the state of the stall, and there is a vortex rollup accompanied by a filled vapor state as can be seen from the table(4.6) and (4.7).

3D simulation of cavitation along spanwise over a NACA0012 at an angle of attack 8° The extension of 2D to 3D is performed by using the *blockMeshDict* file. In domain of the *blockMeshDict* add $y_{max} = 0.45$ and $y_{min} = -0.45$ which is along span wise direction and 10 processor are used to run simulation of 3D cavitation flows. The turbulence model is k- ω sst is used

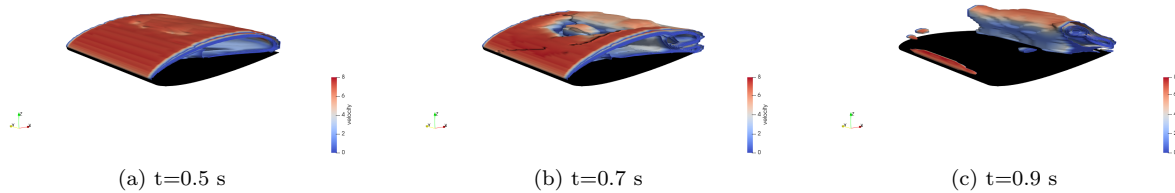


Figure 4.8: 3D velocity distribution over a NACA0012 at different time period

As shown in figure (4.8), a re-entrant jet causes the attached sheet cavity to split along the trailing and leading edges, where the flow is attached. The re-entrant jet moves toward the leading edge at $t=0.5$ s, indicating large-scale cavitation shedding. The attached sheet cavity then collapses at a rate of $t=0.7$ s,

indicating that breaking has begun. In the time interval $t=0.9$ s, the complete shedding can be seen. As shown in figure (4.10), The state will be rolled up and carried downstream once it is vapor-filled and the re-entrant jet was activated to cut the sheet cavity.

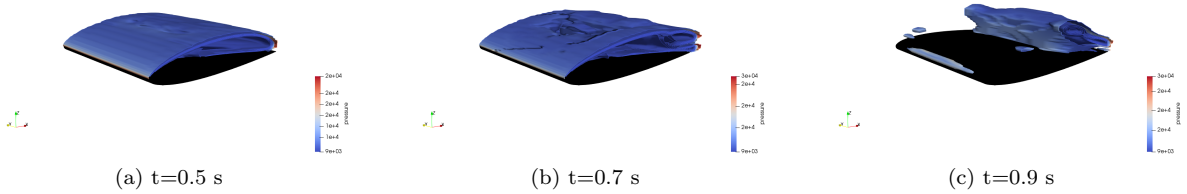


Figure 4.9: 3D pressure distribution over spanwise direction of NACA0012 at different time period

Figure 4.9 shows that the hydrofoil is vapor-filled at $t=0.5$ s, indicating that the state is in stall condition and the suction side of the hydrofoil is at saturation vapor pressure.

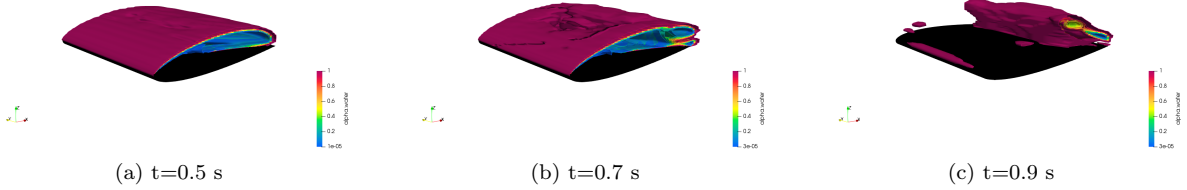


Figure 4.10: 3D alpha.water distribution over spanwise direction of NACA0012 at different time period

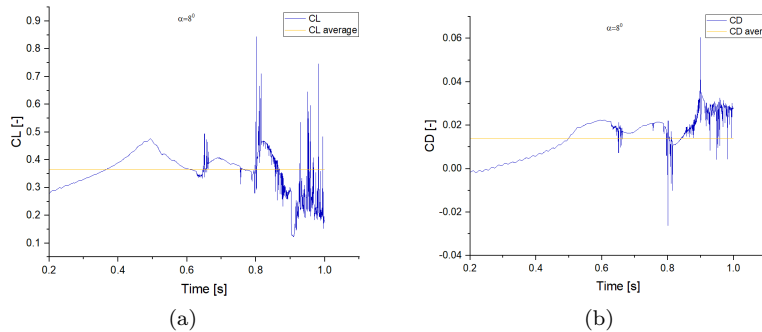


Figure 4.11: 3D, the statistical average of force coefficient over a NACA0012

The CL and CD of a 3D wing at 8° are 0.36 and 0.014, respectively, which is significantly less than the 2D force coefficient mentioned in the table (4.16). This is primarily owing to the simulation's low mesh count. The mesh creation in 3D requires extra attention because it is more complicated than in 2D. However, while both the 3D and 2D models reflect the physics of cavitation shedding, the results are inaccurate due to mesh count and turbulence model selection.

Comparison of numerical and experimental data: The present work data are compared with numerical and experimental data of different authors, are given below:

$\sigma/2\alpha$	Cl Exp	Cd Exp	Cl 1	Cd 1	Cl 2	Cd 2	Cl 3	Cd 3	Cl p	Cd p
2.86	0.595	0.061	-	-	-	-	0.476	0.040	0.818	0.059
3	0.595	0.055	0.580	0.098	0.587	0.039	-	-	0.775	0.051
3.5	0.587	0.045	-	-	0.601	0.030	-	-	0.880	0.029
4	0.577	0.038	0.576	0.086	0.600	0.008	-	-	0.755	0.013
4.5	0.573	0.035	-	-	-	-	-	-	0.590	0.021
5	0.572	0.036	-	-	-	-	-	-	0.535	0.025
5.5	0.573	0.036	-	-	-	-	-	-	0.585	0.023
6	0.574	0.033		-	-	-	-	-	0.543	0.024
6.5	0.573	0.035	0.512	0.028	-	-	-	-	0.505	0.025
7	0.574	0.035	-	-	-	-	-	-	0.472	0.024

Table 4.16: Numerical and experimental result comparision of NACA0012 hydrofoil

Cl p and Cd p is "Force coefficient data of present work". Cl Exp and Cd Exp is "Experimental data given by Takasugi [18]". Cl 1 and Cd 1 is "Numerical data given by Ghassemi [18]". Cl 2 and Cd2 is "Numerical data given by Karim [18]". Cl 3 and Cd 3 is "Numerical data taken from reference [18]".

While comparing the numerical results of the present study with experimental data, from the table (4.9), it appears that from 4.5 to 7, the numerical results are within 10 percent error. Conversely, a numerical result of 2.86 to 4 indicates more than 10 percent error. This means that when dealing with higher angles of attack, special attention needs to be paid to the choice of turbulence model. From the reference paper [18] the numerical data for the value 2.86 is obtained by applying three different turbulence models, such as $k - \omega$ sst, modified $k - \omega$ sst, and LES. Finally, the author concluded that at higher angles of attack it is better to use LES instead of RANS models because the RANS model treat the vortices of different scales equally and this affects the accuracy of the numerical value. Consequently, if we simulate flow at an angle of attack of 4° , it is better to use the modified $k - \omega$ sst because it gives more accurate results with cavitation cloud shedding as stated in reference [18]. Since there is no cavitation shedding when we treat flow at the 4° angle of attack with $k - \omega$ SST as the turbulence model in the present work.

4.3 Concusion

In the present work, $k-\omega$ sst turbulence model is used to study the steady non-cavitation flow and unsteady cavitation flow with cloud shedding over a NACA0012 hydrofoil using interFoam solver in OpenFOAM. The cavitation flows are demonstrated and numerical result are compared with experimental result from [18] and the following conculsions can be drawn:

- In the case of higher angles of attack, it needs further investigation the quantitative analysis because the combination of turbulence model and chosen mesh do not provide accurate quantitative results.
- Realistically, the effect of 3D on experimental results is largely ignored in numerical simulations, which is why this effect shows up as a variation when comparing the numerical result with experiment results.
- In the case of non-cavitating flows, AOA 3.2° to AOA 3.8° , the $k-\omega$ sst model successfully predicts the result with less than 10 percent error when compared to experimental results.
- The $k-\omega$ sst model fails to replicate cloud shedding in cavitating flows, particularly between AOA 4.1° and AOA 5.0° .
- Cloud shedding is observed when the angle of attack is between 5.7° to 8° , and when comparing the numerical result to experimental data, it is clear that the inaccuracy is greater than 10 percent.

- The numerical results are typically reliable in capturing the fracture and detachment behaviors in the cavitation process. But RANS cannot accurately capture the features of the vortices in the flow fields at high angles of attack.

List of Figures

1.1	phase diagram[10]	10
1.2	Andrews-isotherms[10]	10
1.3	Microbubble in liquid [10]	12
1.4	Equilibrium of a sphere nucleus [10]	13
1.5	Schematic of pressure distribution on a streamline[10]	14
1.6	Travelling bubble on the surface of an hydrofoil [10]	15
1.7	ring vortex on the surface of an hydrofoil [10]	16
1.8	Cavitating cloud on hydrofoil [10]	16
1.9	Shear Cavitation [10]	16
1.10	Supercavity behind two dimensional hydrofoil [10]	17
1.11	closure region of partial cavity [10]	18
1.12	Main cavity patterns at $R_e = 2.10^6$ $V_\infty = 10m/s$ on plano-circular hydrofoil [10]	19
2.1	Rayleigh Plesset:Evolution of spherical bubble [10]	23
2.2	Regions of the turbulent boundary layer [14]	28
2.3	Law of the wall [14]	29
3.1	Schematic representation of flow field around 2D NACA0012 hydrofoil with boundary condition	31
3.2	Schematic representation of flow field around 3D NACA0012 wing	32
3.3	Grid lines in coarse mesh over view	33
3.4	rhoPimpleFoam-based solvers	36
4.1	Change in velocity over a NACA0012, non cavitating flow	39
4.2	Change in pressure over a NACA0012, non cavitating flow	39
4.3	alpha.water variation over a NACA0012, non cavitating flow	40
4.4	Change in pressure coefficient over a NACA0012, non cavitating flow	40
4.5	C_p vs x/c for a NACA0012 for non-cavitation flow	40
4.6	Variation of lift and drag coefficient with time on NACA0012, non cavitating flow	41
4.7	Contrast between the pressure distribution of the cavitating and non-cavitating flows	56
4.8	3D velocity distribution over a NACA0012 at different time period	56

List of Tables

3.1	Boundary condition	32
3.2	parameters of work condition	32
3.3	Grid study of AOA 5°	33
3.4	Boundary condition	34
3.5	Parameters in momentumTransport	34
3.6	Parameters in phaseChangeProperties	34
3.7	Parameters in transportProperties	35
3.8	Forces function object	36
3.9	Pressure function object	37
4.1	$\frac{\sigma}{2\alpha}$ and its corresponding α	39
4.2	Velocity distribution in a NACA0012 hydrofoil for an angles of attack ranges from 4.1° to 6.5° and different time period	42
4.3	Velocity distribution in a NACA0012 hydrofoil for an angles of attack ranges from 7.6° to 8° and different time period	43
4.4	Re-entrant jet over a NACA0012 hydrofoil at different angles of attack ranges from 4.1° to 6.5° and time period	44
4.5	Re-entrant jet over a NACA0012 hydrofoil at different angles of attack ranges from 7.6° to 8° and time period	45
4.6	alpha.water distribution over a NACA0012 hydrofoil at different angles of attack ranges from 4.1° to 6.5° and time period	46
4.7	alpha.water distribution over a NACA0012 hydrofoil at different angles of attack ranges from 7.6° to 8° and time period	47
4.8	Pressure distribution over a NACA0012 hydrofoil at different angles of attack ranges from 4.1° to 6.5° and time period	48
4.9	Pressure distribution over a NACA0012 hydrofoil at different angles of attack ranges from 7.6° to 8° and time period	49
4.10	C_p distribution over a NACA0012 hydrofoil at different angles of attack ranges from 4.1° to 6.5° and time period	50
4.11	C_p distribution over a NACA0012 hydrofoil at different angles of attack ranges from 7.6° to 8° and time period	51
4.12	C_p vs x/c graph for different angles of attack ranges from 4.1° to 5.7° and time period . .	52
4.13	C_p vs x/c graph for different angles of attack ranges from 6.5° to 8° and time period . .	53

4.14 Force coefficient at different angles of attack ranges from 4.1° to 5.7° over a NACA0012	54
4.15 Force coefficient at different angles of attack ranges from 6.5° to 8° over a NACA0012	55
4.16 Numerical and experimental result comparision of NACA0012 hydrofoil	58

Bibliography

- [1] R. Bensow and G. Bark. Simulating cavitating flows with les in openfoam. pages 14–17, 07 2010.
- [2] C. E. Brennen. *Cavitation and Bubble Dynamics*. Oxford University Press, 44 edition, 1995.
- [3] C. E. Brennen. *Fundamentals of Multiphase Flow*. Cambridge University Press, 2005.
- [4] J. H. Ferziger, M. Perić, and R. L. Street. *Computational Methods for Fluid Dynamics*. Springer, 4th edition edition, 2020.
- [5] C. J. Greenshields. *OpenFoam User Guide*. OpenFOAM Foundation Ltd, version 9 edition, 2021.
- [6] D. Hai and T. Nguyen. A comparative study of different cavitation and turbulent models of cavitating flow using openfoam. 01 2020.
- [7] V. H. Hidalgo, X. W. Luo, X. Escaler, J. Ji, and A. Aguinaga. Numerical investigation of unsteady cavitation around a naca66 hydrofoil using openfoam. *IOP Conference Series: Earth and Environmental Science*, 22(5):052013, mar 2014.
- [8] V. HIDALGO DIAZ, X. Luo, R. Huang, and E. Cando. Numerical simulation of cavitating flow over 2d hydrofoil using openfoam adapted for debian operating system with lxde based in kernel gnu/linux. *ASME 2014 4th Joint US-European Fluids Engineering Division Summer Meeting collocated with the ASME 2014 12th International Conference on Nanochannels, Microchannels, and Minichannels*, 08 2014.
- [9] A. Inc. *ANSYS FLUENT THEORY GUIDE*. ANSYS, 15.0 edition, 2013.
- [10] J.-M. M. JEAN-PIERRE FRANC. *Fundamentals of Cavitation*. KLUWER ACADEMIC PUBLISHERS, 76 edition, 2004.
- [11] B. Ji, Y. Long, X. ping Long, Z. dong Qian, and J. jian Zhou. Large eddy simulation of turbulent attached cavitating flow with special emphasis on large scale structures of the hydrofoil wake and turbulence-cavitation interactions. *Journal of Hydrodynamics, Ser. B*, 29(1):27–39, 2017.
- [12] B. Ji, X. Luo, R. E. Arndt, X. Peng, and Y. Wu. Large eddy simulation and theoretical investigations of the transient cavitating vortical flow structure around a naca66 hydrofoil. *International Journal of Multiphase Flow*, 68:121–134, 2015.
- [13] K. R. LABERTEAUX and S. L. CECCIO. Partial cavity flows. part 1. cavities forming on models without spanwise variation. *Journal of Fluid Mechanics*, 431:1–41, 2001.
- [14] F. Menter, A. Matyushenko, and R. Lechner. Development of a generalized k-omega two-equation turbulence model. pages 101–109, 01 2020.
- [15] S. B. Pope. *Turbulent Flows*. Cambridge University Press, 2000.
- [16] D. sheng Zhang, W. dong Shi, G. jian Zhang, J. Chen, and B. B. van Esch. Numerical analysis of cavitation shedding flow around a three-dimensional hydrofoil using an improved filter-based model. *Journal of Hydrodynamics, Ser. B*, 29(2):361–375, 2017.

- [17] The OpenFOAM Foundation.
- [18] M. Zhao, D. Wan, and Y. Gao. Comparative study of different turbulence models for cavitational flows around naca0012 hydrofoil. *Journal of Marine Science and Engineering*, 9(7), 2021.